# DEVELOPMENT OF A HIGH-VELOCITY POWDER GUN AND ANALYSIS OF FRAGMENT PENETRATION TESTS INTO SAND

Dwain K. Butler

Army Engineer Waterways Experiment Station
Vicksburg, Mississippi

October 1975

# DISCLAIMER NOTICE

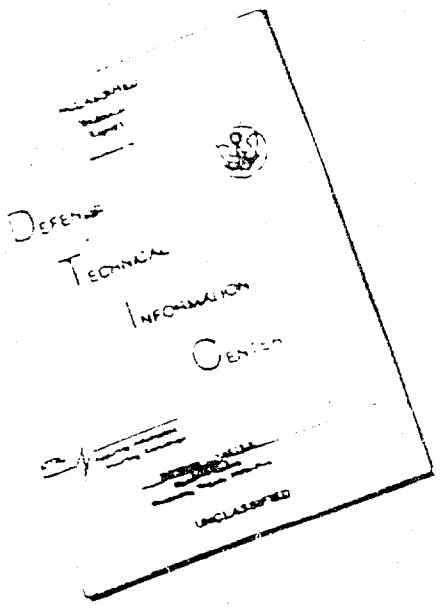


THIS DOCUMENT IS BEST QUALITY AVAILABLE. THE COPY FURNISHED TO DTIC CONTAINED A SIGNIFICANT NUMBER OF PAGES WHICH DO NOT REPRODUCE LEGIBLY.

MISCELLANEOUS PAPER S-75-27

# DEVELOPMENT OF A HIGH-VELOCITY POWDER GUN AND ANALYSIS OF FRAGMENT PENETRATION TESTS INTO SAND

by

Dwain K. Butler

Soils and Pavements Laboratory
U. S. Army Engineer Waterways Experiment Station
P. O. Box 631, Vicksburg, Miss. 39180

October 1975
Final Report



Prepared for Office, Chief of Engineers, U. S. Army
Washington, D. C. 20314

Under Project 4A161102B52E
Task 04, Work Unit 013

Unclassified

SECURITY CLASSIFICATION OF THIS PAGE (When Data Entered)

## REPORT DOCUMENTATION PAGE

READ INSTRUCTIONS BEFORE COMPLETING FORM

| | |
|---|---|
| 1. REPORT NUMBER: Miscellaneous Paper S-75-27 | 2. GOVT ACCESSION NO. |
| 3. RECIPIENT'S CATALOG NUMBER | |
| 4. TITLE (and Subtitle): DEVELOPMENT OF A HIGH-VELOCITY POWDER GUN AND ANALYSIS OF FRAGMENT PENETRATION TESTS INTO SAND | 5. TYPE OF REPORT & PERIOD COVERED: Final report |
| 6. PERFORMING ORG. REPORT NUMBER | |
| 7. AUTHOR(s): Dwain K. Butler | 8. CONTRACT OR GRANT NUMBER(s) |
| 9. PERFORMING ORGANIZATION NAME AND ADDRESS: U. S. Army Engineer Waterways Experiment Station, Soils and Pavements Laboratory, P. O. Box 631, Vicksburg, Miss. 39180 | 10. PROGRAM ELEMENT, PROJECT, TASK AREA & WORK UNIT NUMBERS: Project 4A161102B52E, Task 04, Work Unit 013 |
| 11. CONTROLLING OFFICE NAME AND ADDRESS: Office, Chief of Engineers, U. S. Army, Washington, D. C. 20314 | 12. REPORT DATE: October 1975 |
| | 13. NUMBER OF PAGES: 63 |
| 14. MONITORING AGENCY NAME & ADDRESS(if different from Controlling Office) | 15. SECURITY CLASS. (of this report): Unclassified |
| | 15a. DECLASSIFICATION/DOWNGRADING SCHEDULE |

16. DISTRIBUTION STATEMENT (of this Report)

Approved for public release; distribution unlimited.

17. DISTRIBUTION STATEMENT (of the abstract entered in Block 20, if different from Report)

18. SUPPLEMENTARY NOTES

19. KEY WORDS (Continue on reverse side if necessary and identify by block number)

Fragmentation
Penetration tests (soils)
Powder guns
Projectiles
Sands

20. ABSTRACT (Continue on reverse side if necessary and identify by block number)

A high-velocity powder gun has been developed and is operational in the U. S. Army Engineer Waterways Experiment Station's Fragment Simulation Facility. The gun has many potential applications for study of the effectiveness of various components of fortification systems (such as soil, wood, fabric, concrete, steel, plastic, etc.) in defeating small-arms munitions and fragment-simulating projectiles. This report documents the design of the gun and presents the results of calibration tests (with nominal 3-g fragments)

(Continued)

DD FORM 1 JAN 73 1473 EDITION OF 1 NOV 65 IS OBSOLETE

Unclassified

SECURITY CLASSIFICATION OF THIS PAGE (When Data Entered)

20. ABSTRACT (Continued)

over the velocity range 0.05 to 0.222 cm/μsec. The results of 27 penetration tests of cylindrical fragments into dense sand targets are presented. Results are presented in the form of depth of penetration, fragment frontal enlargement, and fragment mass loss versus impact velocity plots. Comminution of the target material is also studied by performing posttest grain-size analyses for each test. The penetration depth achieved by high-velocity fragments in dense sand is observed not to be a monotonically increasing function of impact velocity but tends to remain constant after a critical impact velocity is exceeded; and the critical impact velocity appears to increase as the strength of the fragment material increases. The phenomenology of the impact-penetration process is discussed in detail. Correlations are established between the grain-size analyses, mass loss data, and frontal enlargement data, and the manner in which these complex phenomena interact is discussed in relation to the penetration depth-impact velocity curve. Finally, it is demonstrated that upper and lower bounds to the penetration depth-impact velocity data can be established in a rational manner with the WES analytical penetration model.

THE CONTENTS OF THIS REPORT ARE NOT TO BE USED FOR ADVERTISING, PUBLICATION, OR PROMOTIONAL PURPOSES. CITATION OF TRADE NAMES DOES NOT CONSTITUTE AN OFFICIAL ENDORSEMENT OR APPROVAL OF THE USE OF SUCH COMMERCIAL PRODUCTS.

# PREFACE

The investigation reported herein was conducted for the Office, Chief of Engineers, U. S. Army, by personnel of the Soil Dynamics Division (SDD), Soils and Pavements Laboratory (S&PL), U. S. Army Engineer Waterways Experiment Station (WES), as part of Project 4A161102B52E, Task 04, Work Unit 013, "Fragment and Projectile Penetration Resistance of Soils."

This investigation was conducted by Mr. Dwain K. Butler during the period December 1973-December 1974, with technical consultation and direction provided by Dr. Behzad Rohani. The high-velocity gun was designed by Mr. Willis J. Dykes, formerly of the Construction Services Division, WES. Assistance with the experimental program was provided by Mr. Leo L. Steen and Mr. Percy L. Collins of the SDD.

The work was performed under the general supervision of Messrs. James P. Sale and Richard G. Ahlvin, Chief and Assistant Chief, S&PL, respectively, and Dr. John G. Jackson, Jr., Chief, SDD.

COL G. H Hilt, CE, was Director of WES during the investigation. Mr. F. R. Brown was Technical Director.

CONTENTS

# DEVELOPMENT OF A HIGH-VELOCITY POWDER GUN AND ANALYSIS OF FRAGMENT PENETRATION TESTS INTO SAND

## PART I: INTRODUCTION

### Background

1. The current analytical and experimental effort at the U. S. Army Engineer Waterways Experiment Station (WES) in penetration of projectiles and fragments into earth materials and concrete stems from a limited research effort initiated in March 1970. Reference 1 presents the results of the initial study, which consisted of a literature review and a preliminary theoretical study of the effectiveness of soil as a fortification material. The purpose of the study was to investigate the feasibility of using the theoretical principles of rupture mechanics and the dynamic constitutive properties of earth materials to establish rational criteria for the design of soil barriers against the effects of conventional explosions, such as high-velocity fragments and airblast.

2. Based on recommendations presented in Reference 1, a coupled experimental and theoretical research program was initiated at WES in August 1970 to study the penetration of high-velocity fragments into soil targets. Using the existing WES Fragment Simulation Facility (FSF), WES engineers conducted an experimental program involving normal impact of right-circular cylindrical fragments (steel and brass) into controlled soil targets (loose sand, dense sand, and clay) at impact velocities between 0.024 and 0.128 cm/usec (800 to 4200 fps). The theoretical portion of the program involved a review of available projectile penetration equations and then an attempt to reproduce the experimental results with a theoretical penetration model based on the theory of dynamic cavity expansion in an elastic-plastic locking medium. In this model, the coefficients appearing in the resulting penetration equations are defined explicitly in

terms of the constitutive properties of the target and the mass and geometry of the projectile. The penetration model was then used to parametrically study the sensitivity of maximum depth of penetration predictions to the descriptive constitutive constants of the targets. It was concluded that the dynamic cavity expansion penetration model can be used to establish rational criteria, based on the constitutive properties of the soil, for predicting or bounding the penetration of high-velocity fragments into soil targets. The results of this research program are presented in Reference 2.

3. Following the experimental phase of the program reported in Reference 2, it was considered desirable to extend the capabilities of the FCF to include impact velocities up to 0.274 cm/μsec (9000 fps), hence making it capable of determining the characteristic shapes of the impact velocity-penetration curves over the entire 0.03- to 0.274-cm/μsec fragment impact velocity range observed in the field. Figure 1 illustrates the penetration depth-impact velocity behavior (over the velocity range of interest) for a hypothetical fragment and target material. There has been considerable experimental study in the low impact velocity range OA for penetration into soils, in which an increasing penetration depth with increasing impact velocity was observed. The data presented in Reference 2 cover the velocity range ABB'C. Curve ABC illustrates the observed behavior of steel fragments penetrating sand, and curve AB'C illustrates the observed behavior of steel fragments penetrating clay and brass fragments penetrating sand and clay. While there have been penetration tests (primarily into sand) in the velocity range CDEFG, they have been conducted at only a few selected impact velocities with a variety of fragment sizes and shapes, and thus it is not possible to deduce the shape of the curve in this velocity range due to the extremely limited experimental data base. It is clearly important with regard to the design of soil fortifications to define the penetration depth-impact velocity curve in the velocity range CDEFG.

4. A high-velocity gun considered capable of producing such a velocity range was constructed, and in December 1973 the experimental program described in this report was undertaken to calibrate and verify the capabilities of the gun and to conduct a limited number of penetration tests into a selected soil target. The details of the penetration depth-impact velocity curve as illustrated in Figure 1 depend not only on the target material but also on the fragment material, geometry, and mass. Dense sand was chosen as the target material for the test series since it appears to offer the best resistance to penetration by high-velocity fragments[2] and exhibits the interesting effect illustrated by curve ABC in Figure 1. Right-circular cylindrical fragments with the same mass as those used in the study reported in Reference 2 were selected with some being of the same type steel. This factor should allow the data of Reference 2 to be extended to higher impact velocities to define the behavior in the range CDEFG.

## Purpose and Scope

5. The purpose of this report is to document the design and capabilities of the high-velocity powder gun which is currently functional in the WES FSF and to present the results and an analysis of 27 fragment penetration tests of small, right-circular cylindrical fragments into dense sand targets.

6. The design and capabilities of the WES high-velocity powder gun facility are described in Part II. Part III describes the experimental program and presents the data obtained from the tests. The data are analyzed and discussed in Part IV. Conclusions and recommendations are given in Part V.

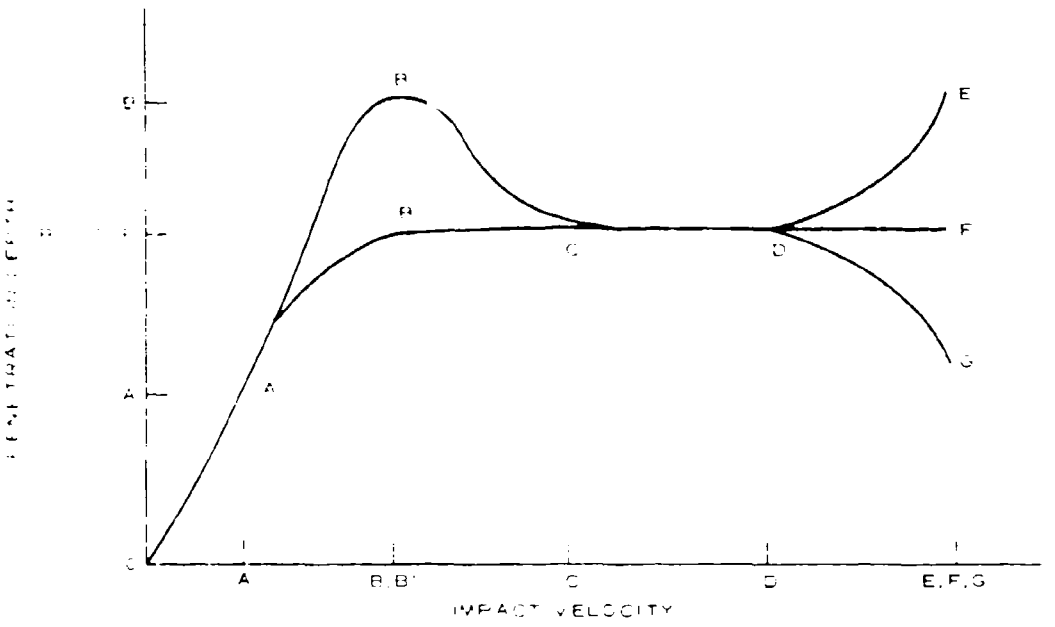


Figure 1. Penetration depth-impact velocity behavior for small fragments into earth media

## PART II: DESIGN AND CAPABILITIES OF THE WES HIGH-VELOCITY POWDER GUN FACILITY

### Fragment Simulation Facility

7. The WES FSF is described in References 2 and 3 and illustrated in Figure 2. The facility consists of an underground firing range, containing the high-velocity powder gun and associated measurement systems, and an adjacent outside support building, containing the firing control, electronic data acquisition systems, and equipment necessary for handloading cartridges and preparing powder charges.

### High-Velocity Powder Gun

8. Figures 3-5 show the high-velocity powder gun. For ease of presentation and discussion, the gun will be considered in five component systems consisting of: (a) bolt-action mechanisms, (b) firing system, (c) pressure chamber, (d) barrel (bore) and support system, and (e) muzzle attachments.

#### Bolt-action mechanisms

9. Low-velocity (LV) system. Two conventional bolt-action mechanisms were adapted for use in the gun design (see Figure 3). The two systems are shown in Figures 6 and 7. The system shown in Figure 6 will be referred to as the LV system and consists of a Winchester Model 70 .458-caliber magnum bolt-action mechanism and an adapter to couple with the pressure chamber and barrel assembly. The adapter for the LV system actually extends completely throughout the pressure chamber and mates directly with the barrel (bore). Fragments and sabots (to be discussed later in this chapter ) fit directly into the end of standard .458-caliber magnum cartridge casings (see Figure 6). The casings are filled with the proper weight of Hercules Red Dot Smokeless Powder to achieve the desired fragment velocity (velocity calibration discussed later in this chapter), and combustion is initiated with

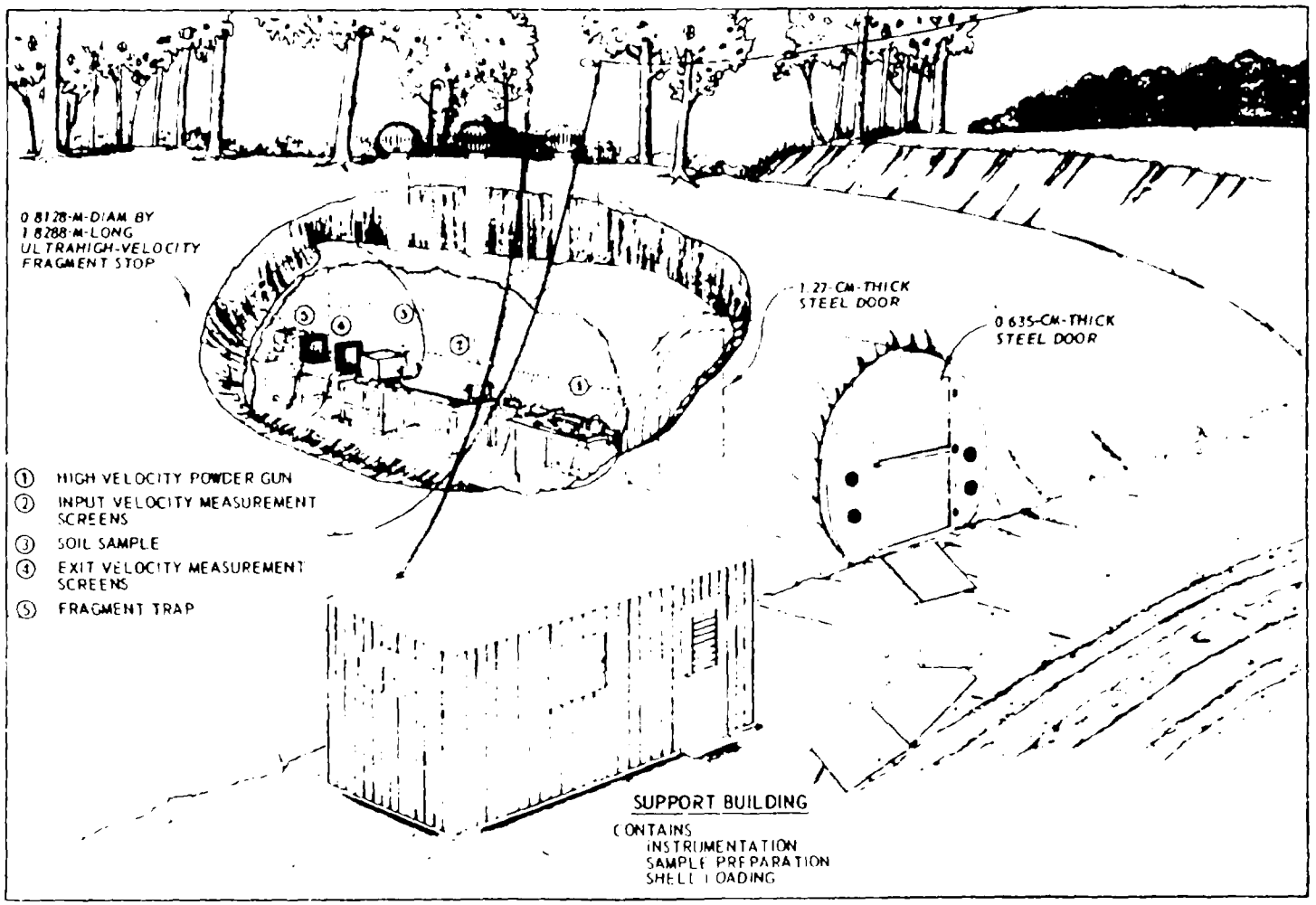


Figure 2. WES fragment simulation facility

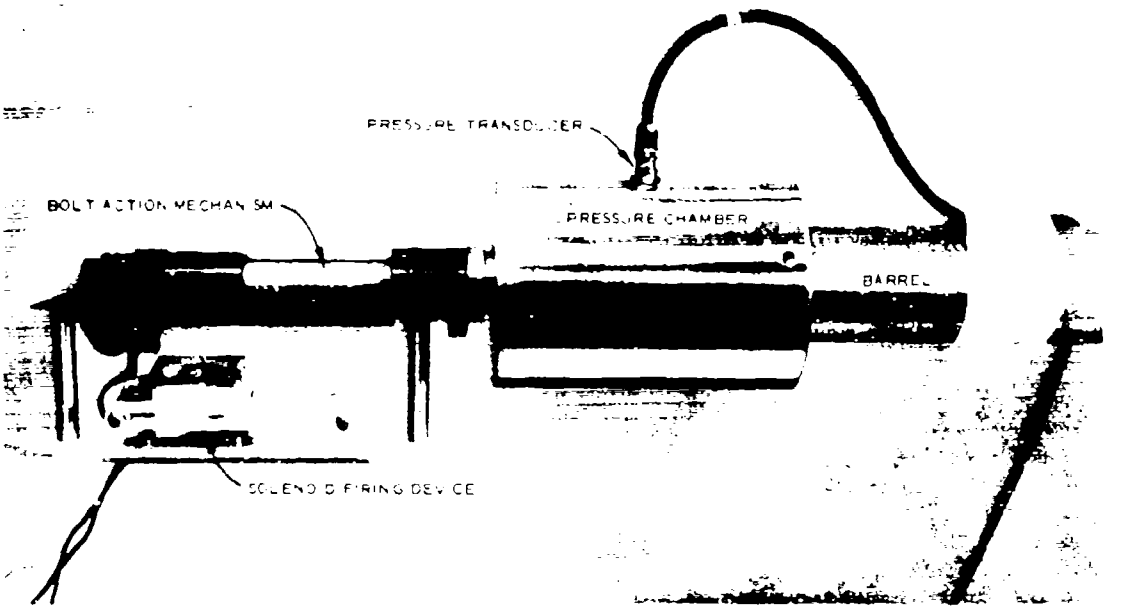


Figure 3. High-velocity powder gun (bolt-action mechanism, pressure chamber, and barrel)

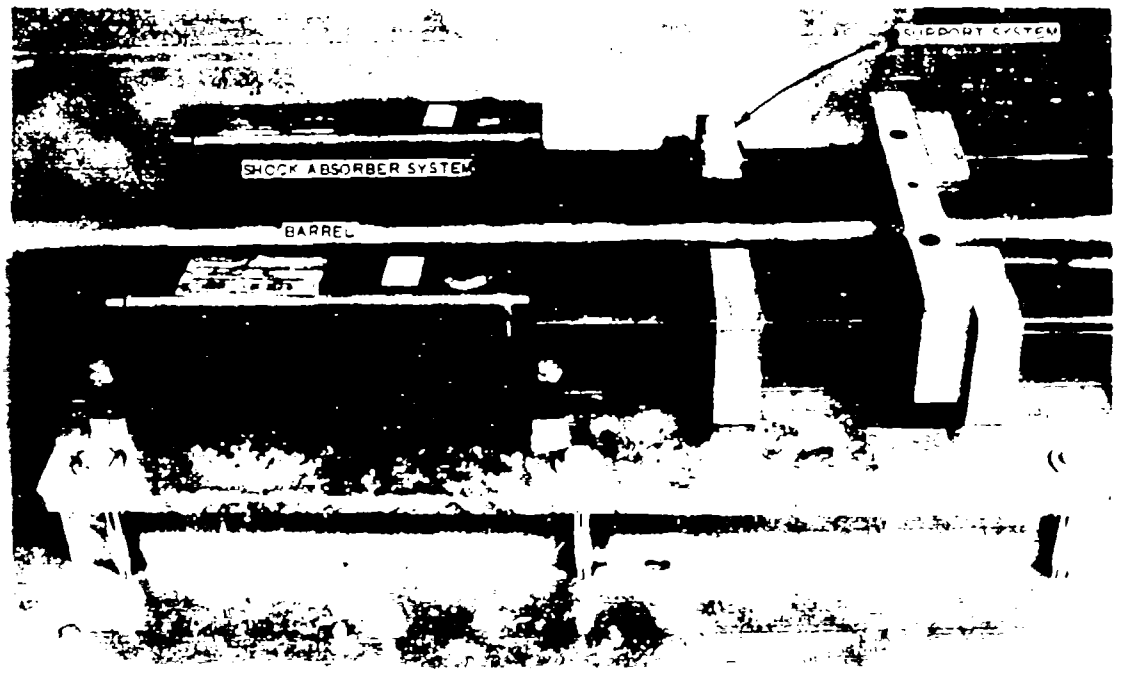


Figure 4. High-velocity powder gun (barrel and support and shock absorber systems)

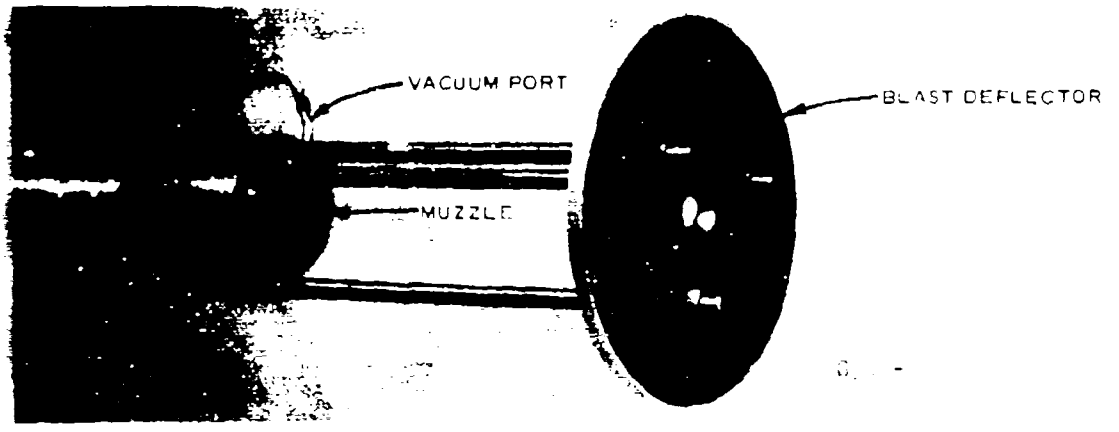


Figure 5. High-velocity powder gun (muzzle, vacuum port, and blast deflector)

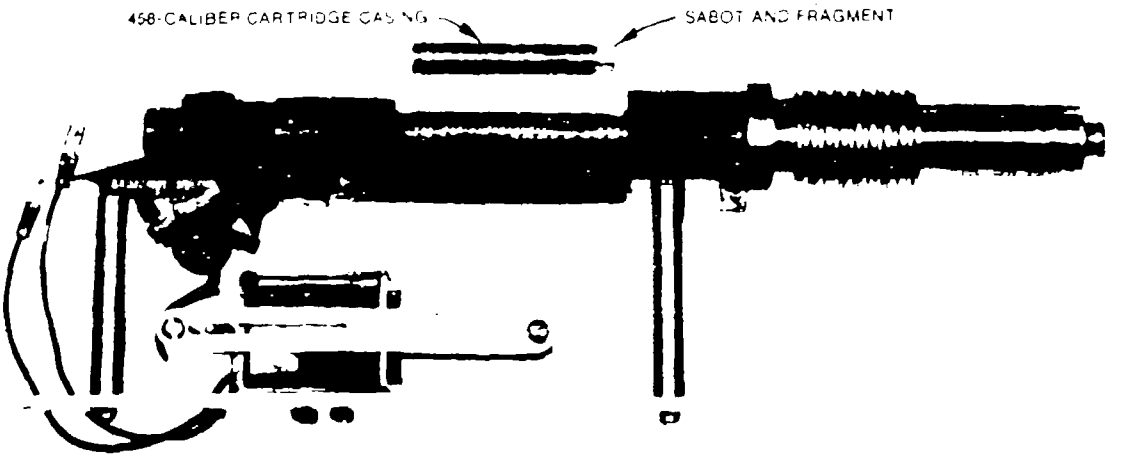


Figure 6. LV system (Winchester Model 70 .458-caliber magnum bolt-action mechanism and coupling adapter)

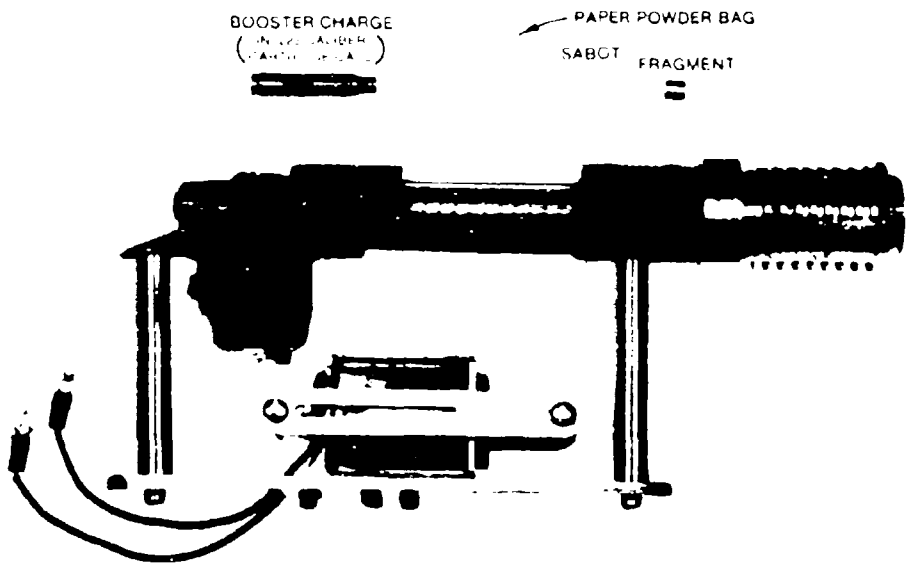


Figure 7. HV system (Remington Model 700 .222-caliber bolt-action mechanism and coupling adapter)

standard rifle primers. This system can produce impact velocities over the range 0.05 to 0.122 cm/μsec for fragments with mass of the order of 3 g.*

10. High-velocity (HV) system. Figure 7 shows the HV system which consists of a Remington Model 700 .222-caliber bolt-action mechanism and an adapter to couple with the pressure chamber. With this system, the gun becomes essentially a two-stage powder gun. The booster charge consists of Red Dot powder confined in a .223-caliber cartridge case by tissue wadding and ignited by a standard rifle primer. High-velocity, high-temperature combustion products are forced through a nominal 0.635-cm-diam orifice in the coupling adapter into the pressure chamber. The primary charge of Hodgdon H870 powder (a very slow burning spherical powder) is contained in the pressure chamber in a paper powder bag (see Figure 7) and is ignited by the stream of combustion products from the booster charge. For this system, the sabot and fragment are placed directly in the rear of the barrel of the gun with a special placement tool. The pressure-time histories in the chamber with this system are discussed later in this chapter. Impact velocities attainable with this system extend from 0.076 to 0.213 cm/μsec.

Firing system and safety considerations

11. Firing is initiated by a firing control switch in the support building. This activates a solenoid device which is mounted on a stage which in turn is attached below the bolt-action mechanisms (see Figures 3, 6, and 7). The solenoid ram impacts the trigger with sufficient force to fire the round. Safety considerations in the firing sequence are simple and straightforward and consist of four essential concepts: (a) all downrange activities such as target preparation, placement of velocity screens, and alignment are completed prior to loading the gun; (b) a safety interlock plug located in the outer chamber of the firing range is pulled

* All fragment velocities given in this report are for nominal 3-g fragments. The velocity range is expected to shift upwards with decreasing fragment mass and downwards with increasing mass.

before entering the inner chamber with the round; (c) the safety of the bolt-action mechanism is kept "on" during the loading operation; (d) the interlock plug is replaced only after closing the inner steel door.

Pressure chamber

12. The pressure chamber is shown in Figure 3 and in section view in Figure 8. The chamber is constructed of AISI 4140 steel (oil quenched) with an elongation to failure in a gage length of 5 cm of 16 percent and an external diameter of 11.43 cm.* During the so-called pyrostatic phase, in which the pressure and temperature increase but the sabot and fragment do not move, and the so-called propulsive phase, in which the lip of the sabot is sheared (using the HV system) and the fragment begins to move, the chamber must withstand pressures possibly as high as 0.0046 Mbar and temperatures as high as 2500 K. The active volume of the chamber is about 41 $cm^3$. A piezoelectric pressure transducer is mounted in the wall of the pressure chamber and is coupled to an oscilloscope in the support building by a Kistler Model 587D Piezotron Coupler for monitoring of pressure-time histories in the active volume of the chamber. With reference to Figure 8, the barrel attaches at the top and the bolt-action mechanism adapter coupling attaches at the bottom.

Barrel and support system

13. The barrel is 252 cm in length, 6.35 cm in external diameter, and 1.163 cm in bore diameter. The sabot and fragment travel approximately 9 cm in freebore and then enter a rifling of one turn in 122 cm. Figure 4 shows the barrel and support system. Gun recoil is absorbed by two EFDYN shock absorbers.

---

* This design should have a factor of safety greater than 3 with respect to tensile failure across section AB (section perpendicular to axis; shown in Figure 8), assuming a maximum chamber pressure of 0.0048 Mbar. A prior chamber constructed of ETD 150 steel with an elongation to failure of 10 percent and an external diameter of 10.16 cm failed catastrophically at section AB at a chamber pressure of 0.0044 Mbar. Since this pressure had been equaled or exceeded prior to the failure case, the failure may have been a fatigue failure.

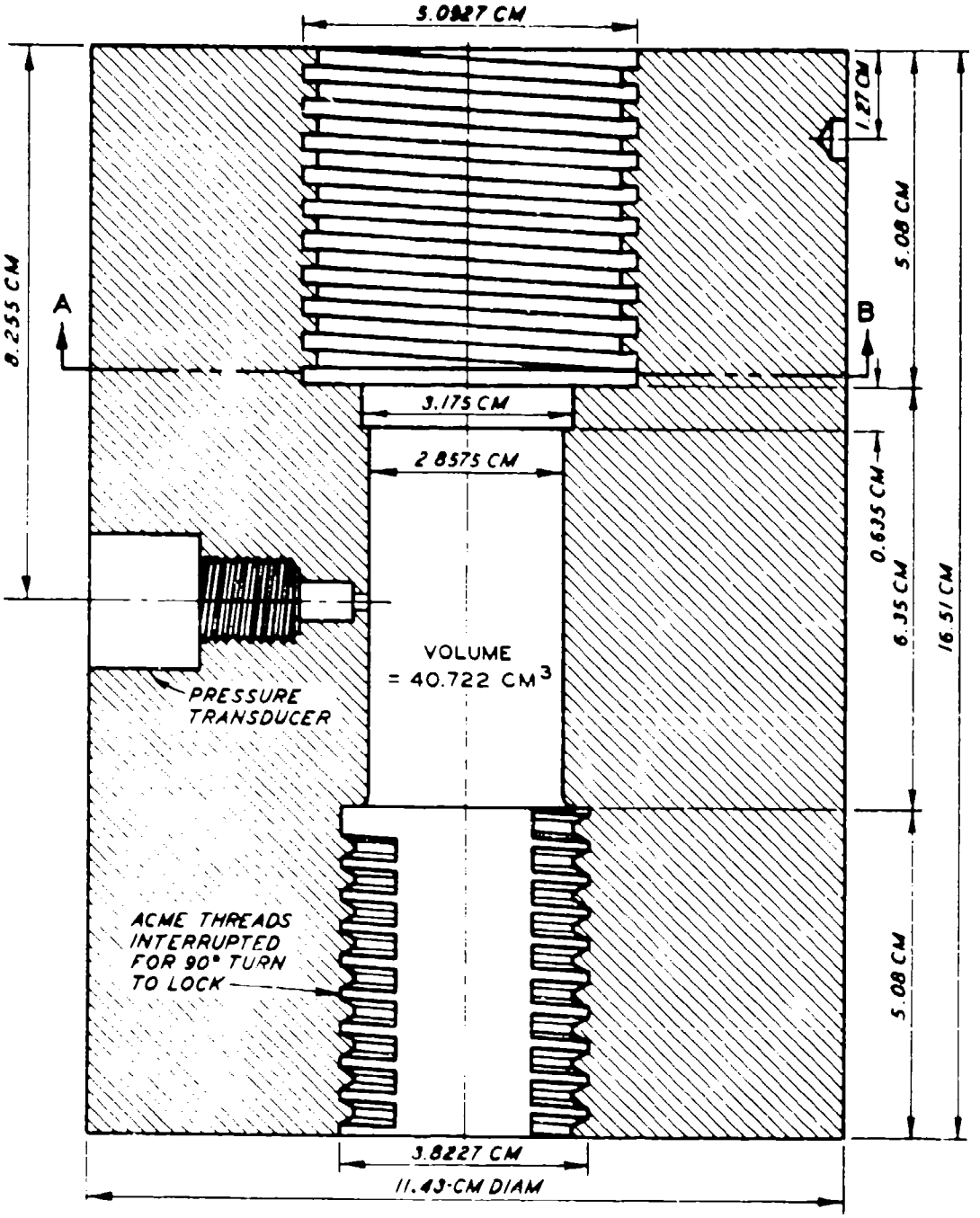


Figure 8. Section view of pressure chamber

Muzzle attachments

14. Figure 5 shows the gun muzzle with the blast deflector and vacuum fitting in place. Not shown is a sabot stripper which attaches to the blast deflector through the central hole. The vacuum fitting screws into the end of the barrel (forming a 2.5-cm extension) and has a port for connection to a vacuum pump and a small recess around the opening into which plastic discs are placed to form a seal. With the HV system, the sabots form a seal at the opposite end of the barrel and the entire bore can be evacuated. The blast deflector is located 28 cm from the muzzle.

## Chamber Pressure Measurements

15. The purpose of monitoring chamber pressure was primarily to avoid exceeding design stresses of the chamber during the preliminary testing and calibration of the gun. Also, the pressure-time records give an indication of the overall efficiency of the gun; for example, one of the early decisions based on pressure-time records was to switch to a very slow burning powder in order to maximize the total impulse while keeping the maximum pressure below design limits. Figure 9 is a pressure-time record for a test with 500 grains of H870 powder, maximum chamber pressure of about 0.0034 Mbar, and a velocity at station 1 (see Figure 10) of 0.2143 cm/μsec.

## Velocity Measurements

16. Velocity is determined by a time-of-flight measurement over a known distance. Two systems are used for the time-of-flight measurements which consist of "triggers" to start and stop counters. The triggers are Oehler Research photoelectric screens and paper screens, and the counters are Oehler Model 20 Digital Chronographs (which record time in microseconds). The counters start when the fragments interrupt

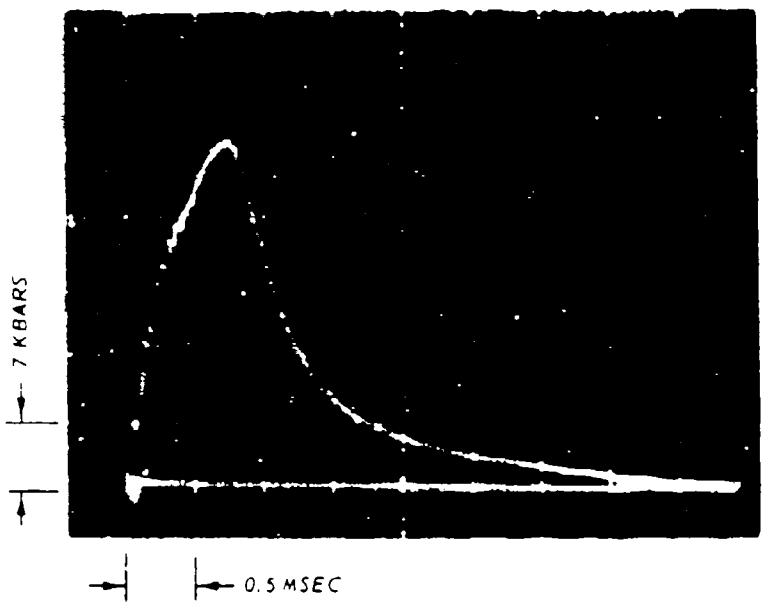


Figure 9. Pressure-time record

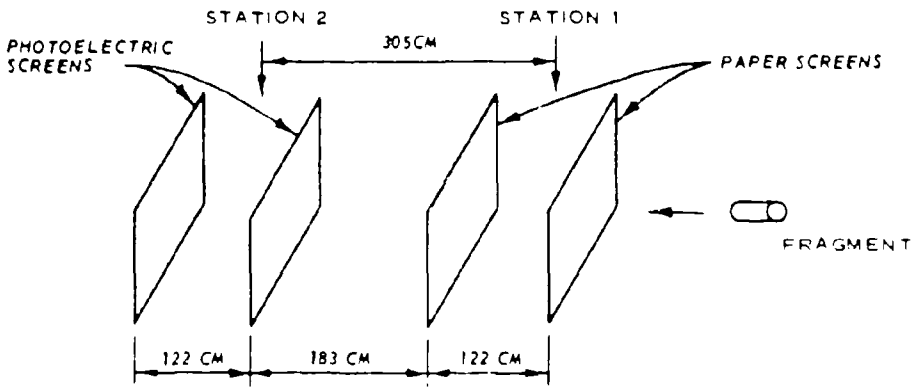


a. GUN CALIBRATION AND DETERMINATION OF THE VELOCITY LOSS CHARACTERISTICS OF FRAGMENT IN AIR

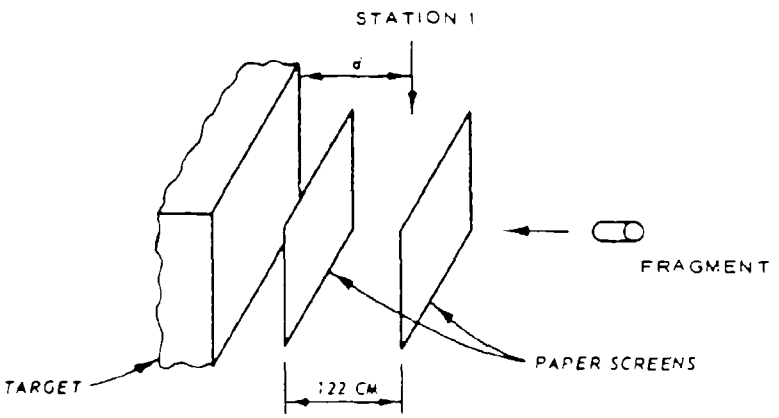


b. IMPACT VELOCITY DETERMINATION

Figure 10. Setup for velocity determinations

the light path in the photoelectric screens or physically break a conducting path consisting of a continuous metallic strip painted on the paper screens. The paper screens are considered more reliable at higher velocities.

17. Figure 10 illustrates the geometry of the test setups used for the velocity calibration of the gun and impact velocity determination. The average velocity over the fixed distance between the two sets of screens is assigned to the midpoints, giving velocities $V_1$ and $V_2$ at stations 1 and 2, respectively (Figure 10a). A number of tests were conducted with both the LV and the HV systems varying the powder charge weights. Figures 11 and 12 are plots of the velocity $V_1$ at station 1 (122 cm from muzzle) versus powder charge weight for the LV and HV systems, respectively. Also shown in Figure 12 are data for a limited number of tests with the bore evacuated, and the general result is an increase in $V_1$ for a given charge weight. The velocity appears to increase with decreasing chamber pressure as would be expected although the limited number of tests and limited capacity of the vacuum pump prevent definitive conclusions. An example of the trend is shown by the following data:

| Charge Weight grains of H870 | Bore Pressure torrs | $V_1$ cm/μsec |
|---|---|---|
| 475 | 760 | 0.1935 |
| 475 | 630 | 0.1992 |
| 475 | 150 | 0.2095 |

It is difficult with the present techniques to obtain a good seal at the muzzle end, and thus the effect of bore pressure cannot be thoroughly studied.

18. The test setup with the target in place is shown in Figure 10b. In this case, only the velocity $V_1$ is determined, while what is needed is the target impact velocity, which is the velocity at a distance $d$ from station 1 (typically 122 cm). To obtain the impact velocity, an adjustment must be made to the measured $V_1$ to account for the velocity loss in air over the distance $d$. Equations 1 and 2 express the

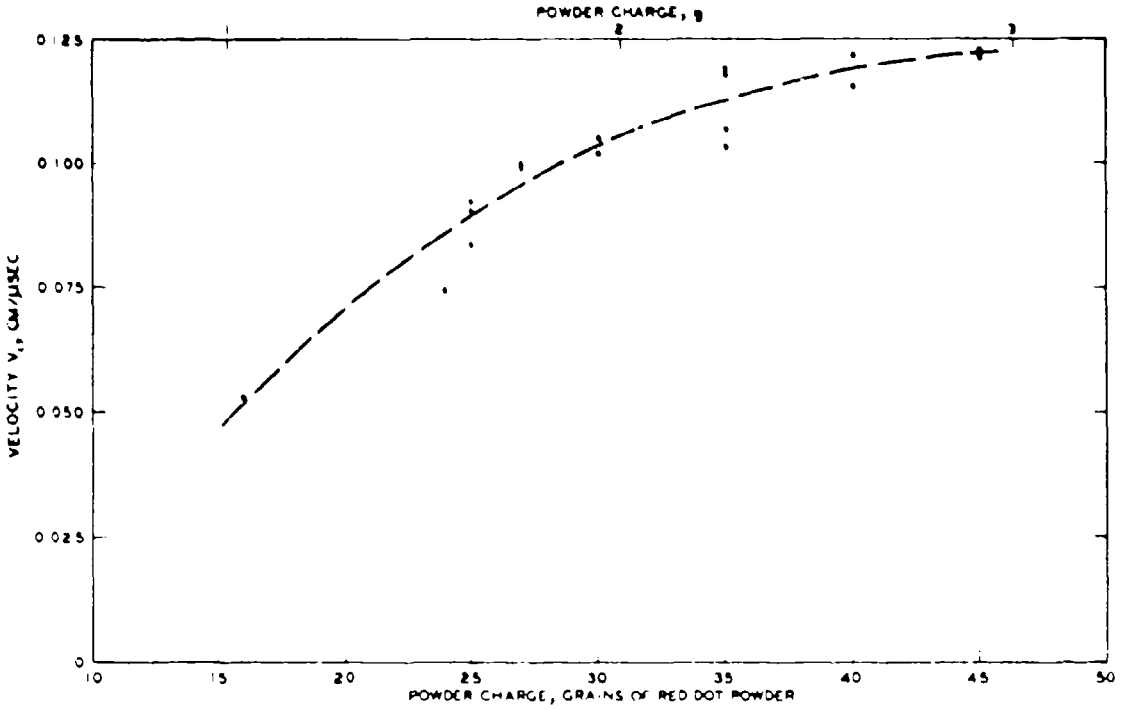


Figure 11. Velocity calibration for LV system (velocity at station 1)

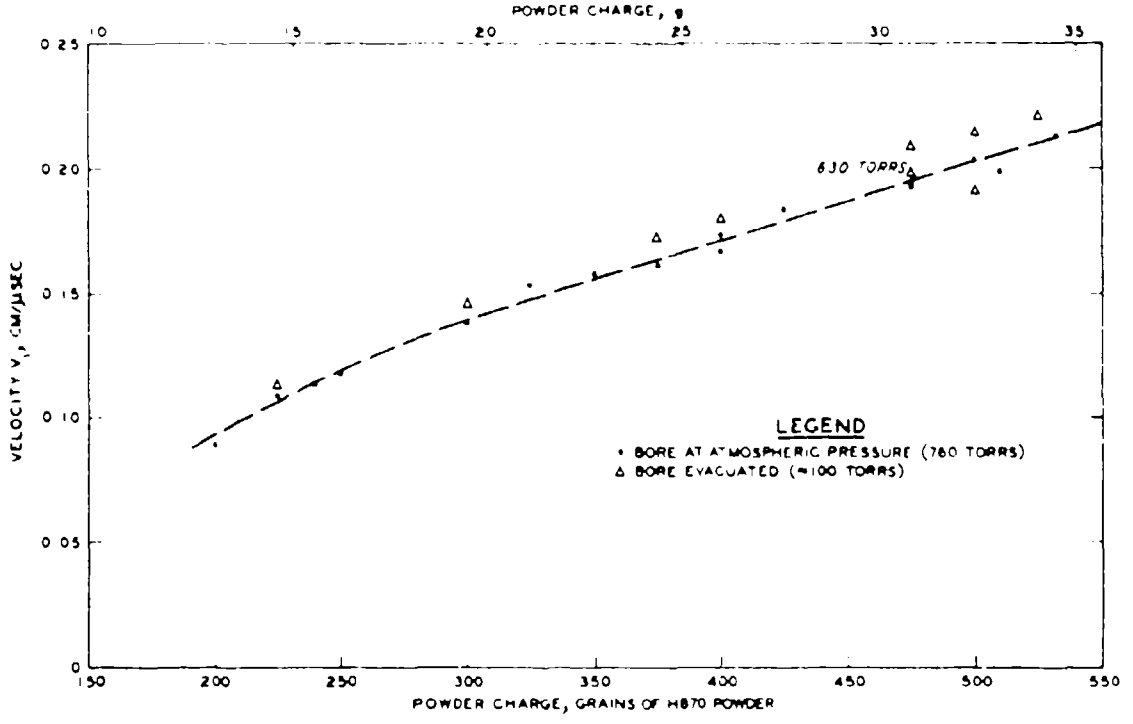


Figure 12. Velocity calibration for HV system (velocity at station 1)

results of observations of velocities $V_1$ and $V_2$ at stations 1 and 2 (separated by 305 cm)

$$\Delta V = V_1 - V_2 = 0.043V_1 \tag{1}$$

$$V = V_1 - \frac{d}{305}\Delta V = V_1(1 - 0.00014d) \tag{2}$$

where

$\Delta V$ = velocity loss for fragment in 305 cm of air, cm/μsec

$V_1$ = velocity of fragment at station 1, cm/μsec

$V_2$ = velocity of fragment at station 2, cm/μsec

$V$ = impact velocity, cm/μsec

$d$ = distance from station 1 to target, cm

## Sabots and Fragments

19. Sabots are devices which carry the fragments down the gun bore and make it possible to use fragments not cylindrical in shape and smaller in maximum dimension than the bore diameter. Figures 6 and 7 show the types of sabots and fragments used in this study. The sabots were constructed of lexan (polycarbonate) and machined to form a tight fit in the bore in order to contain the high-pressure combustion products as the sabot and fragment are accelerated. In order to facilitate the separation of the sabots from the fragments after they emerge from the muzzle, the sabots were slotted at 90-deg intervals around the circumference. Sabot separation presented some difficulty, and future programs should devote more effort to sabotry.

## PART III: EXPERIMENTAL PROGRAM

### Description of Test Program

20. The experimental program consisted of 27 fragment penetration tests into dense sand targets. Data collected from each test consisted of impact velocity, depth of penetration, initial and final fragment dimensions, initial and final fragment masses, sand target density, and grain-size analyses before and after the penetration event. Two series of tests were conducted, both into dense sand targets. In the first series, steel fragments were fired using the LV system, and in the second series, brass fragments and two types of steel fragments were fired using the HV system.

#### Dense sand targets

21. A fine sand, known locally as Cook's Bayou sand, was used for the targets. This sand is well documented and was used as a target material, in both loose and dense states, in an extensive series of penetration tests reported in Reference 2. The material is classified as SP in the Unified Soil Classification System, and the gradation curve is shown in Figure 13. The targets were constructed in plywood boxes of known volume (a cube with 30.48-cm sides) by placing the sand into the box in 10-cm layers. Following the placement of each layer, the box was lifted about 5 cm off the floor and dropped. This procedure was repeated 10 times per layer. The boxes were slightly overbuilt and the excess screeded off. This procedure consistently produced targets with densities in the range 1.66 to 1.76 $g/cm^3$. The front of the box (impact side) contained a 10- by 10-cm cutout in the plywood covered by a thin layer of cardboard, and the top was left open.

#### Fragments

22. Right-circular cylindrical fragments were used in the study. Pertinent properties for the three fragment materials used in the study are listed in the tabulation below.

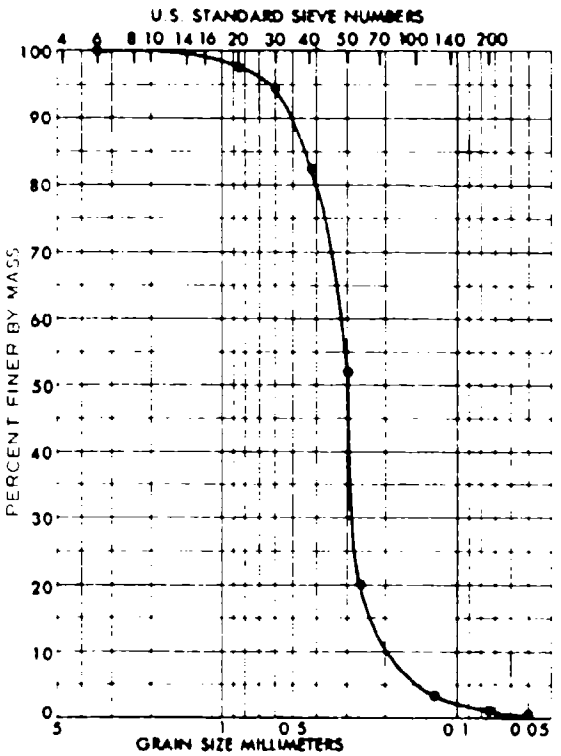


Figure 13. Gradation curve for Cook's Bayou sand

| Metal | Length L, cm | Diam D, cm | Mass M, g | Density g/cm$^3$ | Static Yield Strength $\sigma_Y$, Mbar | BHN* | $\frac{4M}{\pi D^2}$ g/cm$^2$ |
|---|---|---|---|---|---|---|---|
| Steel (SAE 1020) | 0.80 | 0.787 | 3.00 | 7.71 | 0.0035 | 160 | 6.17 |
| Steel (AISI C-1141) | 0.78 | 0.78 | 2.87 | 7.70 | 0.0068 | 252 | 6.01 |
| Brass (ASTM B-16) | 0.78 | 0.78 | 3.00 | 8.05 | 0.0026 | 110 | 6.28 |

* Brinell Hardness Number.

Stress-strain diagrams for the two steels are shown in Figure 14 (unconfined compression tests).

Recovery of fragments

23. Typically four targets were prepared and penetration tests conducted before the fragments were recovered and penetration depths measured. Following the tests, a commercial-type vacuum cleaner was used to excavate the sand from the targets down to the depth of the fragments. Great care was exercised not to disturb the fragment or any of the comminuted sand along the penetration track. The penetration depth was measured by inserting a small rod from the front of the target along the track until it encountered the rear of the fragment. To the depth as measured by the rod was added the measured final fragment length to give the reported penetration depth. Following the depth measurements, the fragments were recovered and paper cups used to obtain the comminuted sand along the track for later grain-size analysis.

## Test Results

24. The test results are presented in Tables 1 and 2 and include the impact velocity $V$, penetration depth $P$, target density, frontal area enlargement coefficient $C_A$, and reduced mass coefficient $C_M$. The coefficients $C_A$ and $C_M$ define the enlargement of the frontal area of the fragment due to plastic deformation and the loss of mass due to erosion, respectively.

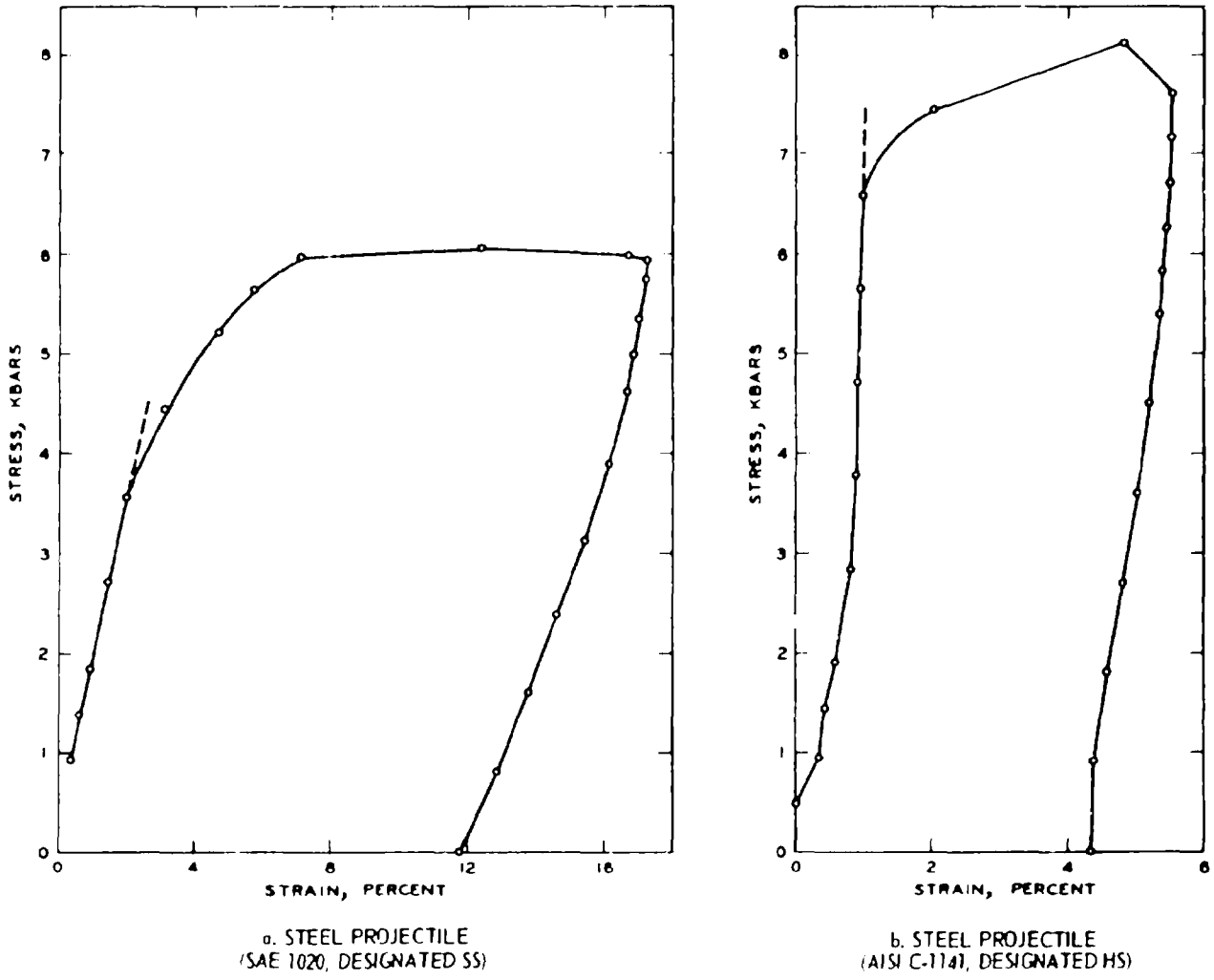


Figure 14. Results of unconfined compression tests of steel fragments used in test program

$$C_A = \frac{A_f}{A_i} \tag{3}$$

$$C_M = \frac{M_f}{M_i} \tag{4}$$

where

$A_f$ = frontal area of fragment after penetration event*

$A_i$ = initial frontal area

$M_f$ = mass of projectile after penetration event

$M_i$ = initial mass

The test numbers identify the fragment materials as SS (soft steel, $\sigma_Y$ = .0035 Mbar), HS (hard steel, $\sigma_Y$ = .0068 Mbar), and B (brass); the target material as DS (dense sand); and give a LV or HV series number. Thus, SS-DS-LV2 indicates a penetration test into dense sand with a soft steel fragment that is the second test in the series of tests using the LV system. The test results are plotted in Figures 15-17. Results of the grain-size analyses will be presented and discussed in Part IV.

---

* The frontal area following the test is determined from a mean diameter determination (the result of several dial caliper measurements).

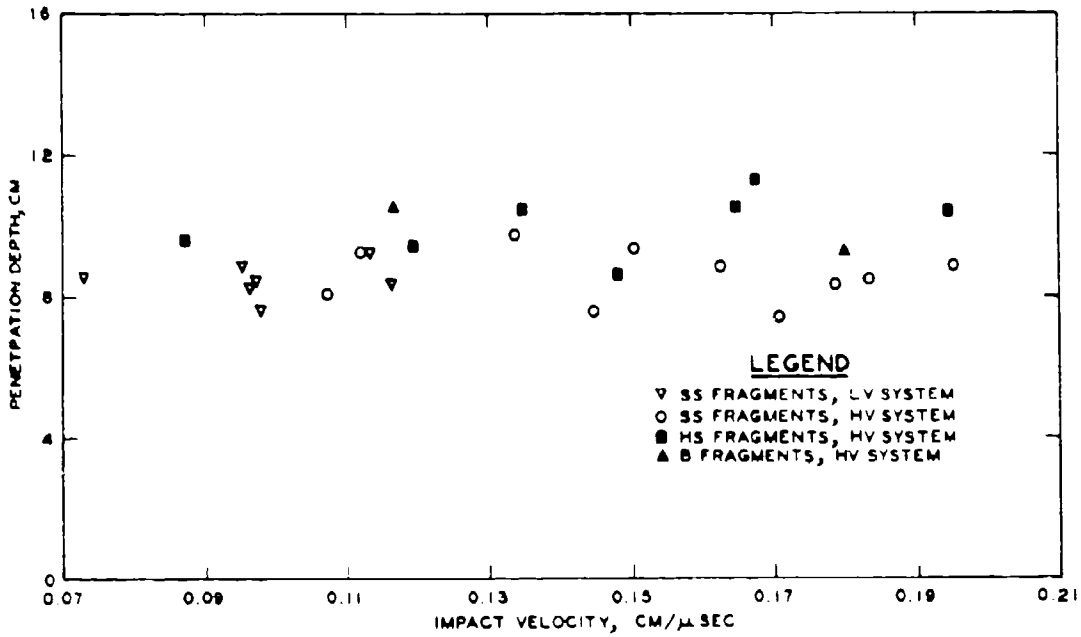


Figure 15. Projectile penetration into dense sand

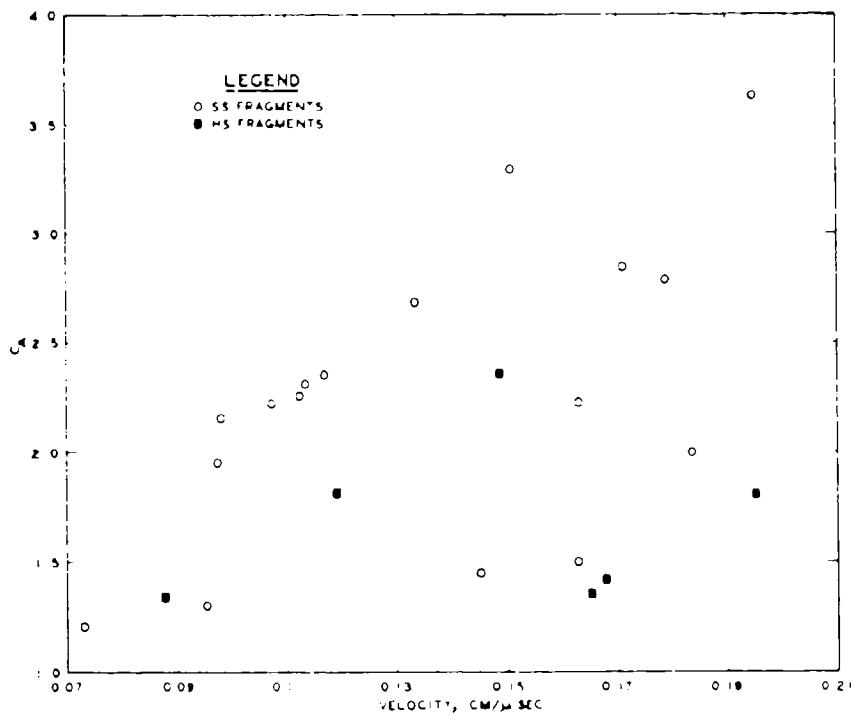


Figure 16. Frontal area enlargement coefficient versus impact velocity

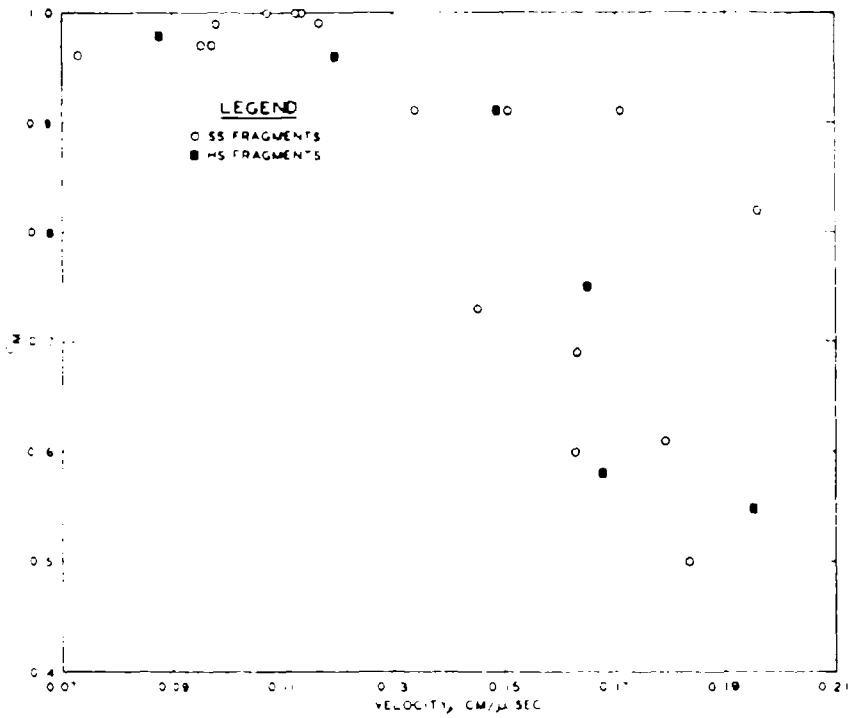


Figure 17. Reduced mass coefficient versus impact velocity

## PART IV: ANALYSIS AND DISCUSSION OF EXPERIMENTAL PROGRAM

### Projectile Penetration Depth, Deformation, and Mass Loss

#### Analysis of results

25. It is evident from Figures 16 and 17 and the data in Tables 1 and 2 that in none of the penetration tests conducted did the fragment penetrate as a rigid body of constant mass. In all cases, the fragments deformed, and in all but three cases, mass was lost during the event. Figures 18-20 illustrate the typical appearance (with a magnification factor of 3) of the fragments following penetration into the dense sand. It was concluded in Reference 2 that, in the rigid penetration range in which the fragments undergo only elastic deformations and no mass loss, the depth of penetration is independent of the yield strength of the material composing the fragment and that penetration depth increases continuously with increasing impact velocity. The data presented in Reference 2 indicate that the rigid penetration range for steel fragments (same material as the HS fragments in the study reported here) terminates at impact velocities of 0.0762 to 0.0914 cm/μsec (2500 to 3000 fps) in dense sand. Thus, the range of impact velocities in this study is above the rigid penetration range.

26. The penetration depth versus impact velocity data of Figure 15 for all three fragment materials are contained within a horizontal band about 4 cm in width. Penetration depths achieved by the SS fragments appear to be slightly smaller over the investigated impact velocity range than those for the HS fragments. For comparison purposes only, best-fit straight lines to the data for the SS and HS fragments are shown in Figure 21. The data for the SS fragments are scattered about a constant penetration depth of about 8.6 cm. The fit for the HS fragments indicates greater penetration depths, but the slight increase in penetration depth with increasing impact velocity should be viewed with caution due to the small number of data points.

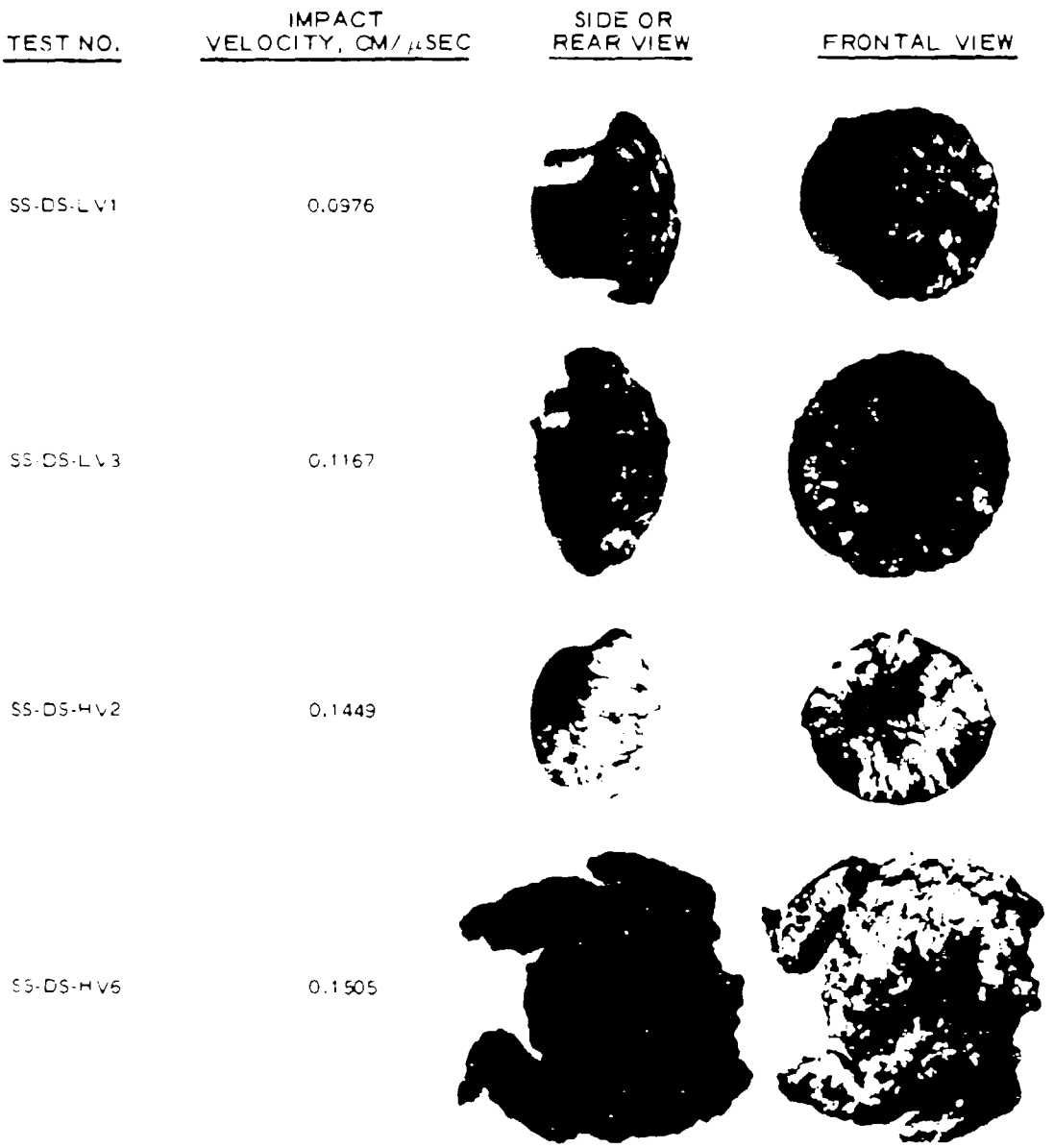


Figure 18. SS fragments following penetration into dense sand

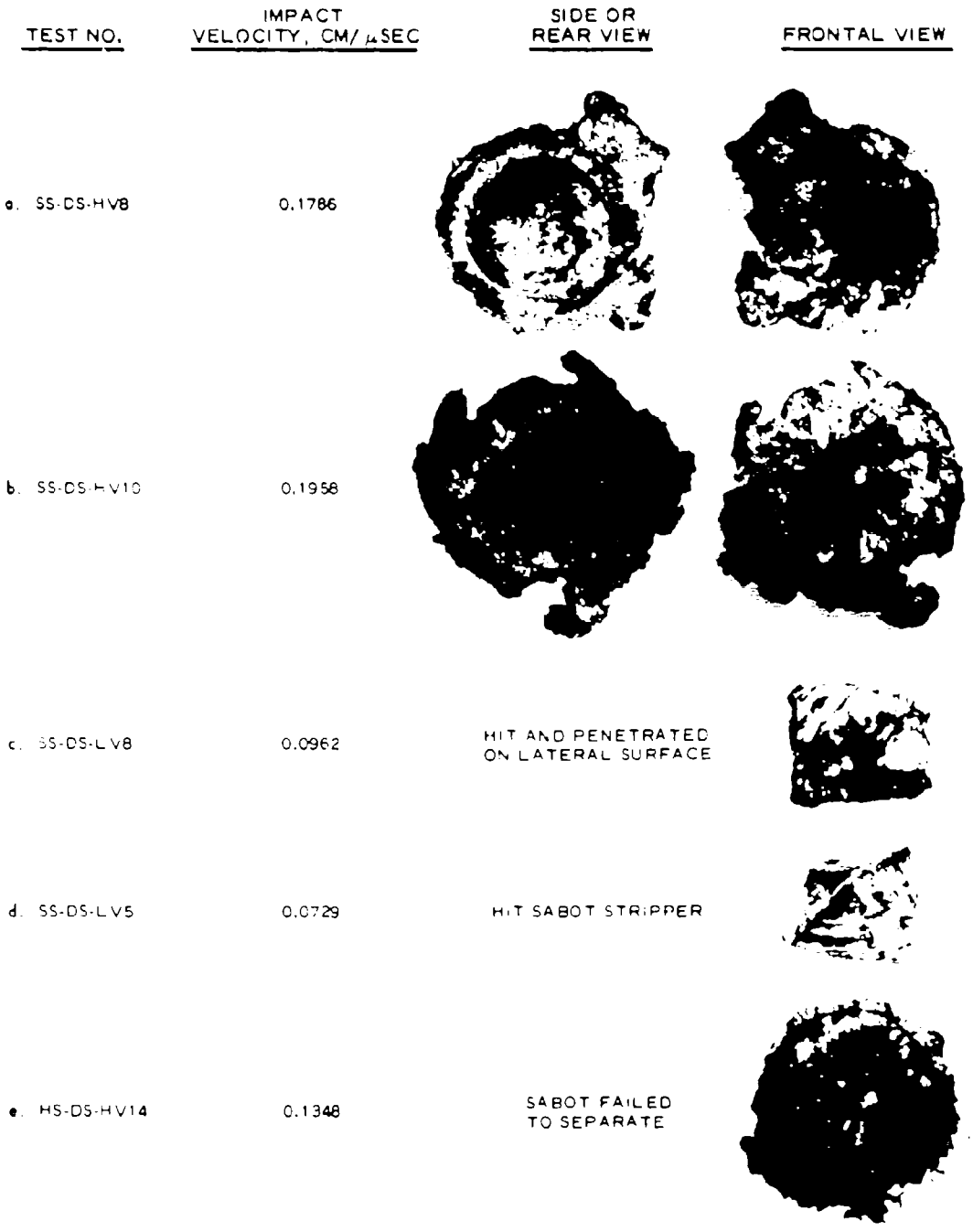


Figure 19. SS fragments (a and b) and nontypical SS and HS fragments (c-e) following penetration into dense sand

| TEST NO. | IMPACT VELOCITY, CM/μSEC | SIDE OR REAR VIEW | FRONTAL VIEW |
|---|---|---|---|
| HS-DS-HV13 | 0.0878 | | |
| HS-DS-HV12 | 0.1194 | | |
| HS-DS-HV11 | 0.1481 | | |
| HS-DS-HV15 | 0.1648 | | |
| HS-DS-HV16 | 0.1946 | | |

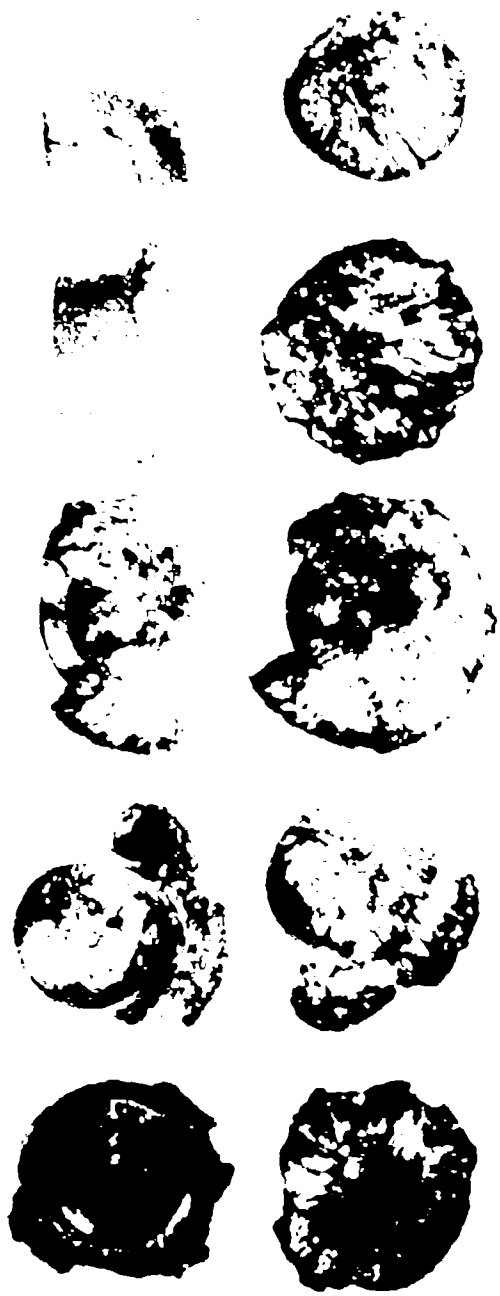

Figure 20. HS fragments following penetration into dense sand

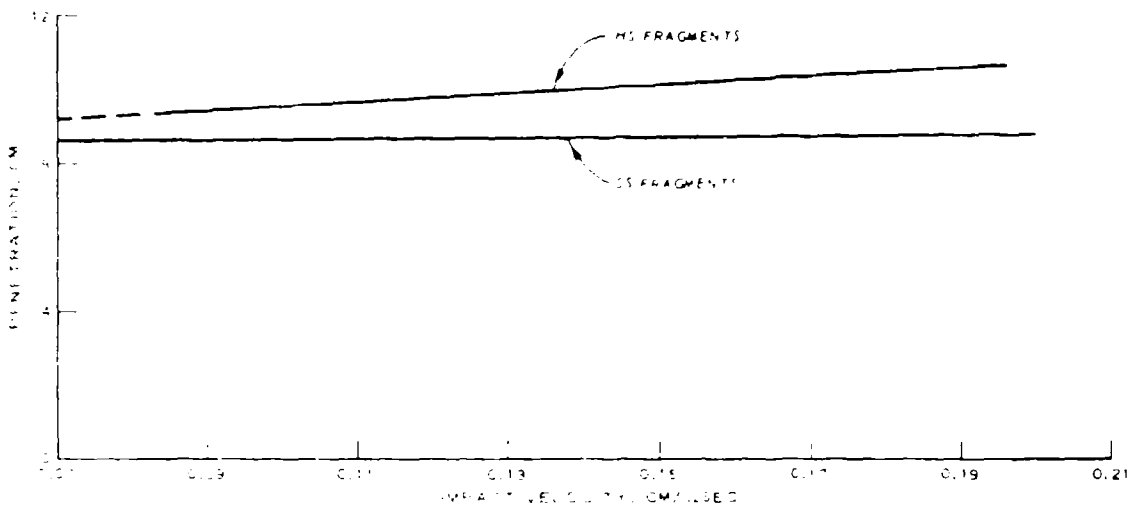


Figure 21. Best-fit straight lines to penetration data

27. Figure 22 compares the data from Reference 2 for dense sand penetration with data from the tests in this study for HS fragments. Except for the data point for test No. HS-DS-HV13 (impact velocity of 0.0878 cm/μsec), the data from the tests in this study correlate quite well with the higher velocity data from Reference 2 and thus appear to form a logical extension for the dense sand penetration of this type steel (HS) fragment to impact velocities of 0.20 cm/μsec (6500 fps). The drop in penetration depth at impact velocities between 0.09 and 0.11 cm/μsec in the data from Reference 2 is neither confirmed nor refuted by the present test results, since the variance of the one data point below 0.11 cm/μsec could be explained simply by data scatter or, as can be seen in Figure 20, by the fact that the axis of the fragment was probably not perpendicular to the impact surface at impact and during penetration. It is demonstrated in Reference 4 that, for long rod penetration, it is theoretically possible to have a decrease in penetration depth with increasing impact velocity. It is interesting to note that the general shape of the penetration versus impact velocity curve (say a best-fit curve to the data) of Figure 22 closely resembles the curves of Reference 4 for cases in which the strength of the target is less than the strength of the fragment.

28. Only two penetration tests were conducted with brass fragments. The penetration depth for test No. B-DS-HV19 agrees with the data for brass penetration into dense sand of Reference 2. An impact velocity of 0.18 cm/μsec represents about the maximum impact velocity for which a recognizable piece of brass fragments of the type used in this test program can be recovered. This fact is evident from the very small value of $C_M = 0.16$ for test No. B-DS-HV20.

Phenomenological discussion

29. Following impact, plane shock waves propagate into the target and fragment with magnitudes which depend on the impact velocity and the material properties of the target and fragment. The plane shocks are quickly distorted and attenuated due to rarefaction waves from

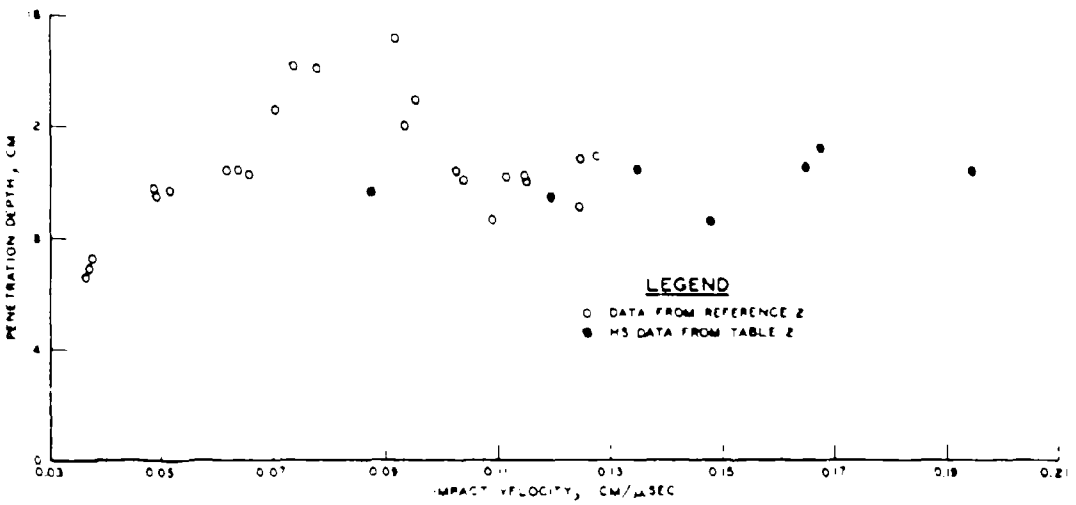


Figure 22. Comparison of data from Reference 2 with data for HS fragments in this study penetrating dense sand

lateral and rear surfaces of the fragment and from the "free" surface of the target. The rarefaction waves from the lateral fragment surface will generate tensile stresses in the fragment which, if the dynamic yield strength of the fragment material is exceeded, will tend to cause plastic deformations and lateral material flow (radial flow). It is this mechanism which produces the familiar, characteristic mushroom shapes shown in Figures 18-20.

30. Thus, as impact velocity increases above a critical velocity (the impact velocity for which stresses in the fragment exceed the yield stress), plastic flow will occur and continue until stresses fall below the yield stress (which itself may have changed during the event). At high impact velocities, the frontal area will not only increase but the fragment will lose mass as the "mushrooming" material separates. For impact and penetration into sand, mass is also lost due to the abrasive action of the sand grains on the fragment, and this effect should increase in importance as the impact velocity increases and as the yield strength and hardness of the material composing the fragment decrease.

31. In general, the penetration depth depends directly on the fragment mass and inversely on the presented frontal area (perhaps to some power). The diagrams in Figure 23 illustrate in section view the geometries of the recovered fragments for increasing impact velocity. It is hypothesized that the diagrams can also be considered as a time sequence of events in the penetration process for an impact velocity $V_6 > V_c$ (see Figure 23f), where the dashed lines in Figure 23d represent incipient separation of the "mushrooming" material. Figure 24 presents hypothetical plots of $C_A$ and $C_M$ versus impact velocity. $C_A$ remains constant at 1.0 until $V_c$ is exceeded and then increases in some monotonic manner until a velocity $V_5$ is reached, at which point the separation indicated in Figures 23d and 23e occurs and a sudden drop in $C_A$ occurs. At some low velocity (not necessarily $V_c$), mass begins to be lost due to erosion and

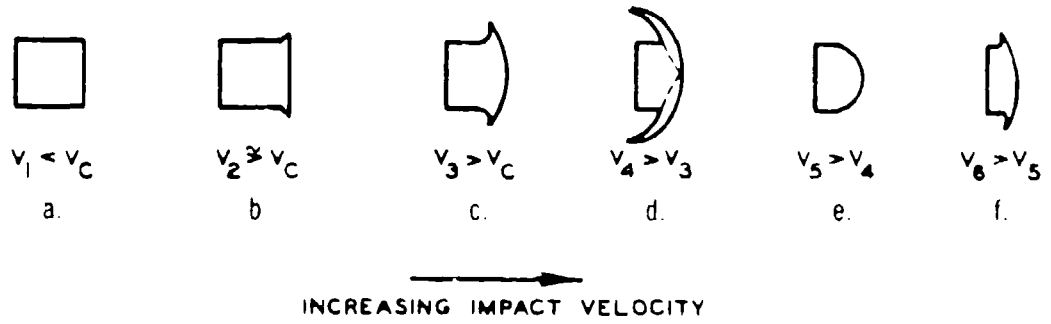


Figure 23. Cross-sectional views of fragments following penetration at increasing impact velocities $V_i$ ($V_C \equiv$ critical impact velocity for plastic flow)

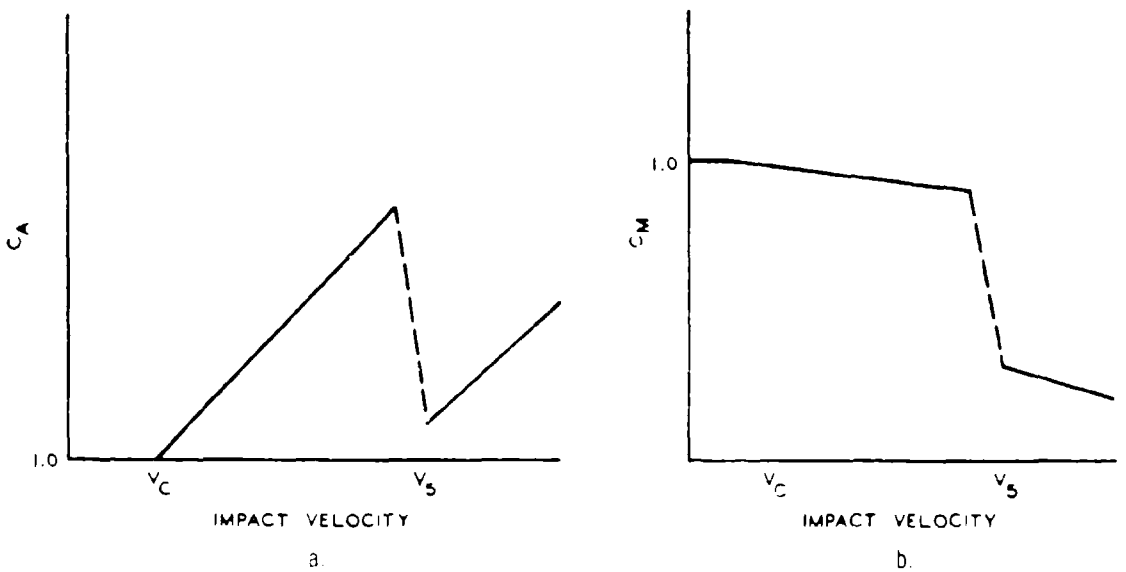


Figure 24. Hypothetical plots of $C_A$ and $C_M$ versus impact velocity for the phenomena represented in Figure 23

continues throughout the impact velocity range. This loss is indicated by the negative slopes in Figure 24b. The sudden drop in $C_M$ at $V_5$ again corresponds to the separation indicated in Figures 23d and 23e.

32. For a number of tests, a magnet was used to recover steel from the comminuted sand samples. Typical appearance of the recovered steel is shown in Figure 25 for both the HS and SS fragment tests. The recovered steel from both type projectiles contained rather large curved platelike pieces indicative of the mechanism proposed in Figure 23d. In general, the pieces of the SS fragments were larger than those of the HS fragments, as would be expected due to the lower yield strength and greater ductility of the SS material. Also, the edges of the HS fragments were drawn thinner and had a more jagged, striated appearance (this effect might be indicative of strain hardening; see Figure 14b). Very small pieces of the fragments such as might result from the abrasive action of the sand were present following tests with both types of steel.

33. Evidences of high temperatures during the penetration process were the "charred" appearance of the fragments, recrystallization, and a noticeable elevation in temperature of large volumes of the target. Also present in the recovered pieces of the HS fragments were grayish-black spherules ($\leq$1 mm in diameter) which could have been formed only by complete melting. An X-ray diffractogram revealed that the spherules contained $\alpha$-iron and quartz. Also, the diffractogram contained a broad maximum, characteristic of an amorphous solid, at a position near that typically observed for the glass of the specimen slides. Indeed, the broad maximum may have been due to the glass slide as the small amount of material caused the prepared specimen to be transparent in places. However, an intriguing possibility is that the maximum could be an indication of the presence of elemental silicon in an amorphous form. This possibility is suggested by the presence of iron oxide on some of the pieces of the steel fragments. Thus, it is possible that the penetration process provided the extreme reducing environment

a. RECOVERED SS b. RECOVERED HS

Figure 25. Posttest recovered steel from comminuted sand surrounding fragment track

necessary for the reaction $Fe_3O_4 + 2Si \rightarrow 3Fe + 2SiO_2$ to occur in the reverse direction.[5] Further analyses with larger quantities of the spherule material are necessary to define conclusively its composition and establish a minimum velocity for formation of the spherules.

## Sand Comminution and Grain-Size Analyses

34. Comminution (crushing) of sand grains has commonly been observed in standard laboratory testing of sands.[6,7] Application of confining pressures (isotropic compression) above a threshold value results in a shift of the grain-size distribution (gradation) curve of a test sample. At a given confining pressure, application of shearing stresses results in a further and relatively larger upward shift in the grain-size distribution curve. Similar shifts in gradation curves have been observed for dynamic laboratory tests on sands, and sand comminution has been observed in fragment penetration tests and considered in analyses of penetration tests into sand.[8-12] For a given fragment, a minimum impact velocity exists below which sand comminution does not occur to a significant extent.[8,10] Thompson[11] has observed the formation of "sand cones" on the noses of projectiles with blunt, hemispherical, and ogival nose geometries. The sand cone is formed of compacted,

comminuted sand which adheres to the fragment and moves through the target media as part of the fragment once it has formed. The comminution process is undoubtedly very complex for the fragment penetration case (consisting of comminution caused by the initial shock wave, abrasion between grains caused by shearing motions as the sand is pushed aside, abrasion caused by contact between individual grains and the fragment itself, etc.).

35. A grain-size analysis for the Cook's Bayou sand (parent material) used for the dense sand targets was presented in Figure 13. Figures 26-28 present grain-size analyses for the comminuted sand material obtained from the fragment tracks following the tests.

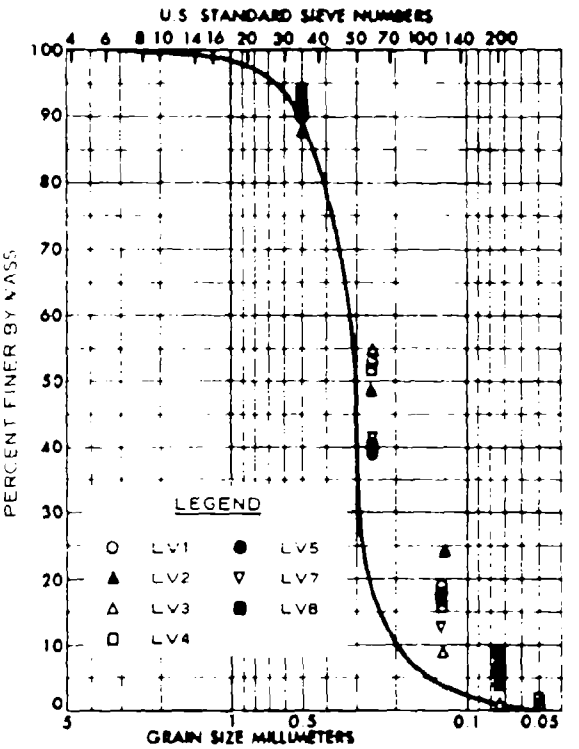


Figure 26. Grain-size data for test Nos. SS-DS-LV1 to -LV8

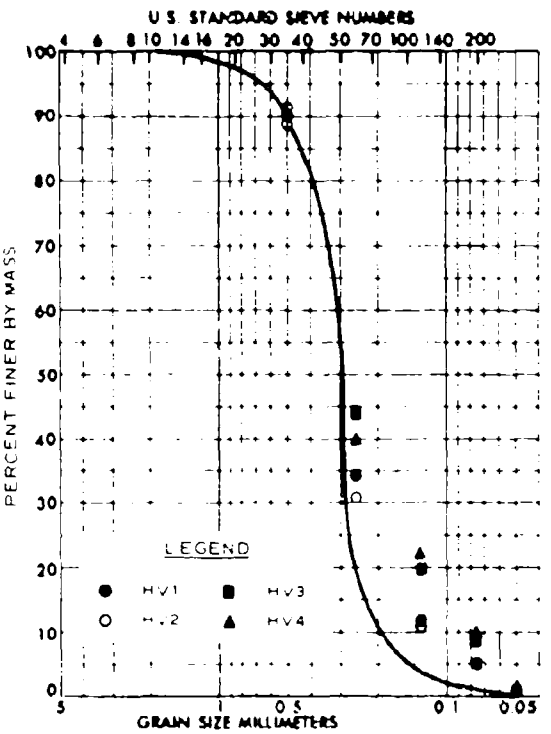


Figure 27a. Grain-size data for test Nos. SS-DS-HV1 to -HV4

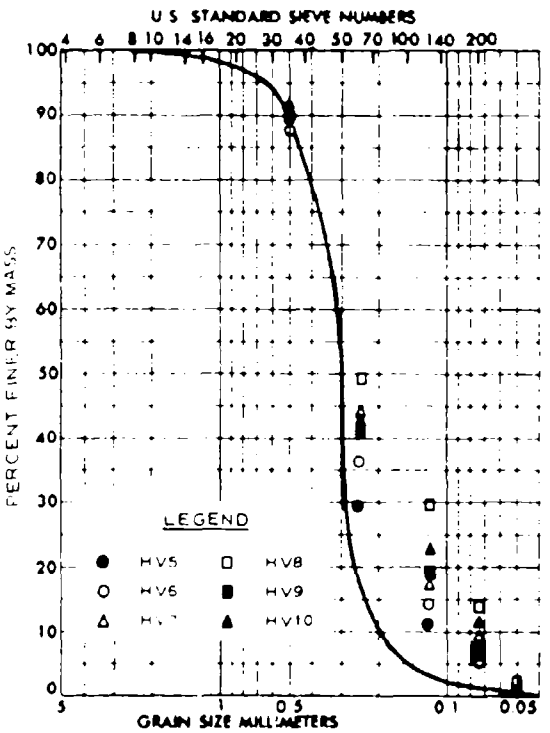


Figure 27b. Grain-size data for test Nos. SS-DS-HV5 to -HV10

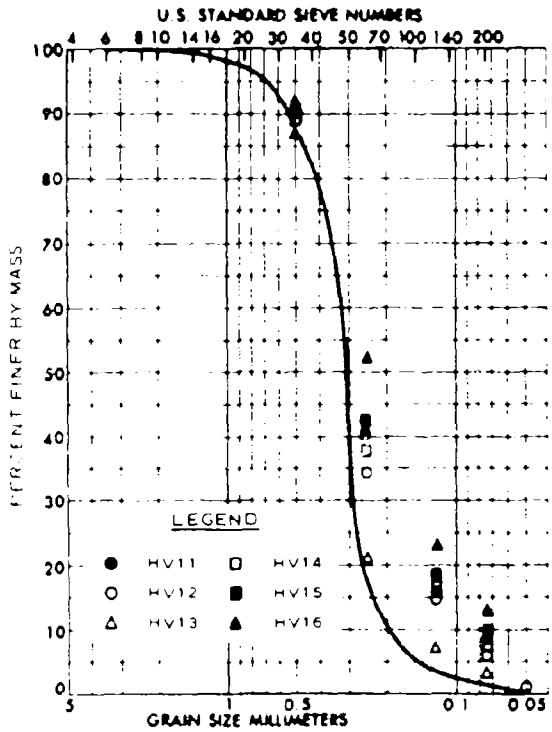


Figure 28. Grain-size data for test Nos. HS-DS-HV11 to -HV16

Each figure contains the curve for the parent material, and the data for each test (for each grain size) are indicated by different symbols. The sampling technique was changed following test No. SS-DS-LV8,* and thus the data for the SS fragments tests are presented in two separate figures (Figures 26 and 27). Figure 28 shows the data for the HS tests.

36. The shifting of the gradation curves from the parent material curve is obvious in Figures 26-28. In order to illustrate more explicitly the effect of impact velocity on grain-size distribution, the percent finer by mass data for three selected grain sizes (0.25, 0.125, and 0.074 mm) are plotted in Figures 29 and 30 for the SS and HS fragment tests, respectively. The points on the percent finer axis for zero impact velocity are for the parent material. Both figures indicate large increases in percent finer by mass for all three grain sizes over the velocity range. A large jump in the percent finer by mass values is evident in Figure 30 at an impact velocity of about 0.10 cm/μsec. It is interesting and significant to note that this is about the velocity at which the dramatic decrease in penetration depth occurs in the composite data plot in Figure 22 and also about the velocity at which a significant increase in the frontal enlargement coefficient is observed (Reference 2 and Figure 16). The data in Figures 29 and 30 do not confirm but are consistent with the concept that comminution does not occur below a minimum impact velocity. It is tempting, but would be too much a matter of conjecture at this point, to interpret each of the increases and decreases in the percent finer versus impact velocity data in Figures 29 and 30 in terms of the mechanism proposed in Figures 23 and 24 and the $C_A$ and $C_M$ data

---

* For the SS tests with the LV system, material was collected only from around the terminal position of the fragments and the samples averaged about 20 g in mass. For the remainder of the SS tests and all the HS tests (with the HV system), an attempt was made to recover all the comminuted material along the fragment track, and the samples averaged about 100 g in mass.

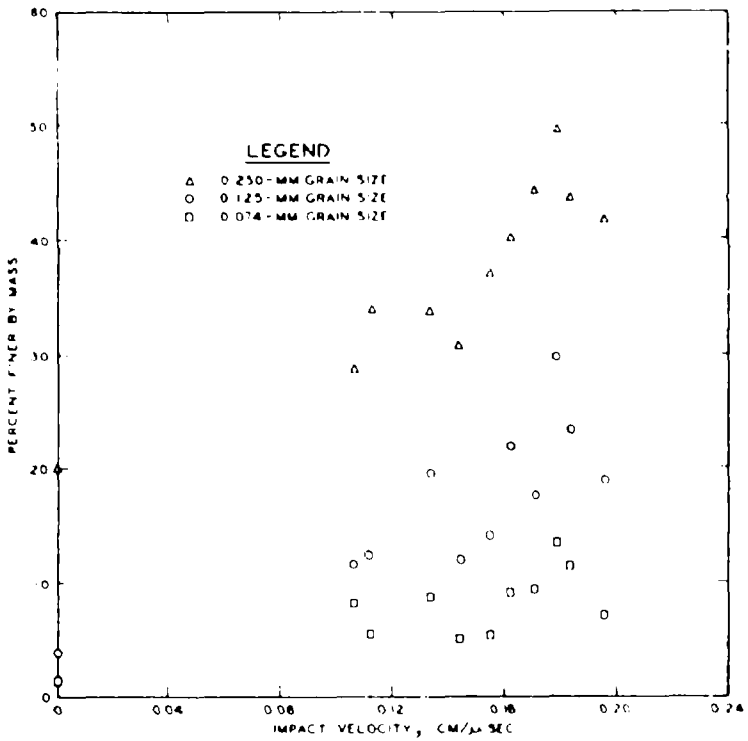


Figure 29. Percent finer by mass at three selected grain sizes versus impact velocity for SS fragment tests with HV system

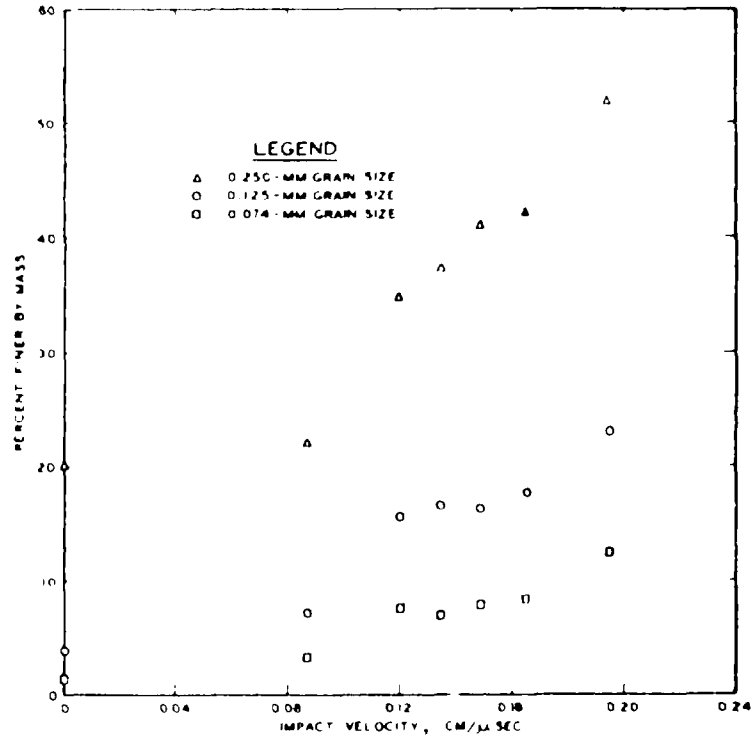


Figure 30. Percent finer by mass at three selected grain sizes versus impact velocity for HS projectiles

in Figures 16 and 17. If such an interpretation could be substantiated by further and more refined penetration tests and grain-size analyses, it would represent a significant advancement in the understanding of the energy exchange mechanisms operating during the impact and penetration process.

37. Some evidence of sand cone formation was present on a few of the recovered fragments, but in none of the cases was a "complete" sand cone observed or recovered as discussed by Thompson[11] for larger diameter projectiles. It is possible that the complex mass loss and frontal enlargement mechanisms, proposed earlier for the small blunt fragments used in these tests, prevented the formation of other than temporary sand cones (small fragments of compacted, comminuted sand were observed along some of the fragment tracks). The grain-size data are representative of some type of average gradation along the length of the fragment tracks. The actual grain sizes do not abruptly terminate at 0.05 mm as the figures might suggest, since in several cases in excess of 0.5 g of material passed a No. 300 (0.05-mm) sieve and as much as 0.1 g passed a No. 325 (0.044-mm) sieve. Mechanical sieving is not a reliable technique for determination of grain sizes smaller than a No. 200 sieve size, and it was observed that even after an hour of sieving, in some cases, the separation process was not complete.

## Correlation of Phenomenological Observations with Dynamic Yield Strengths of Fragment Materials and Energy Partitioning Considerations

38. Taylor[13] has demonstrated that the profile of a cylindrical rod following impact with a rigid boundary can be related to the dynamic yield strength of the material composing the rod. In a more recent study, Wilkins,[14] based on the method proposed by Taylor, simulated the impact of rods, of several material types and length-to-diameter ratios varying from 1 to 15, into a rigid boundary with an elastic-plastic finite difference computer code. He also conducted experimental impact

tests and demonstrated that the observed rod profile after impact for a given impact velocity can be duplicated in the code calculations by varying the yield strength parameter; then, using the yield strength parameter for which the profile has been duplicated, the profiles following impact at different impact velocities can also be duplicated. The yield strengths deduced by this procedure agree quite well with previously published values determined by plane shock wave experiments[15,16] and rod penetration tests.[17] Butler[18] has demonstrated that measurements of fragment deformations, following penetration into an explosive simulant material, can be used to deduce the dynamic yield strength of a fragment by using the data to deduce the critical impact velocity for deformation and then using graphical impedance matching techniques to determine the impact pressure.

39. The pressure and particle velocities in the fragment and target at impact can be estimated by simple methods such as graphical impedance matching or by using the method of characteristics to solve the boundary value problem existing at impact (both methods are based on a one-dimensional hydrodynamic analogy of the fragment impact).* Figure 31 illustrates pressure versus relative density relations for fragments and sand targets.[2,9,19] Using these relations, a computer code based on the method of characteristics was used to solve the one-dimensional analogy of the fragment-target impact to obtain the impact pressure-impact velocity and particle velocity-impact velocity relations shown in Figure 32.

40. Based on the data presented in Reference 2 and in Figure 16, critical impact velocities for deformation of the HS and SS fragments were estimated to be 0.06 and 0.042 cm/usec, respectively. From Figure 32, the code calculations for these impact velocities give 18 and 11 kbars for the dynamic strengths of the HS and SS materials, respectively. The dynamic strength value of 11 kbars for the SS fragment material (SAE 1020 steel) correlates quite well with dynamic yield

* The article by Duvall in Reference 12 discusses the validity of the one-dimensional hydrodynamic approximation.

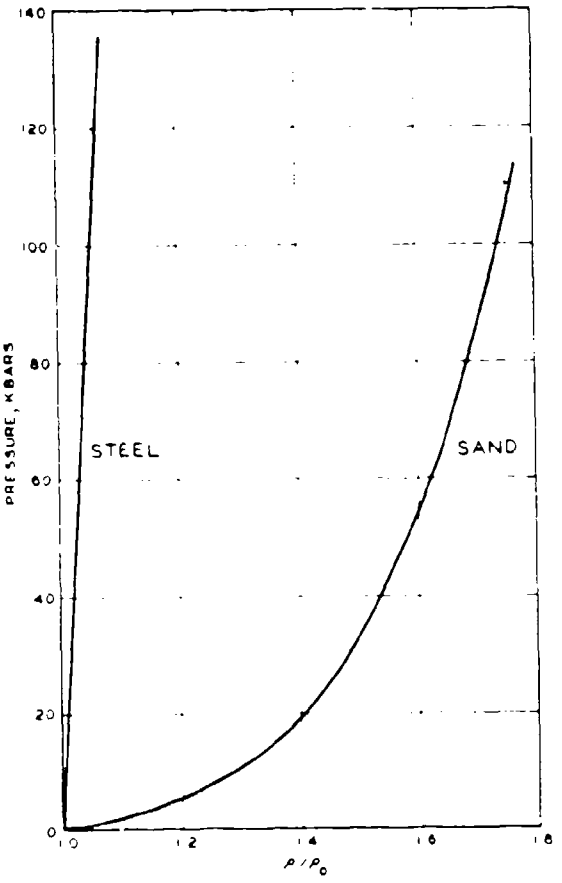


Figure 31. Pressure versus density relation for steel and sand

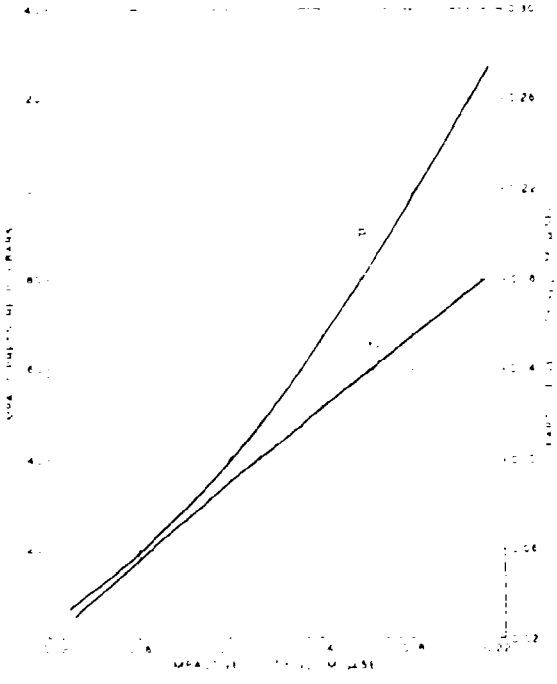

Figure 32. Impact pressure and particle velocity in target versus impact velocity

strength values of 12.8 and 10.4 kbars for two thicknesses of SAE 1020 steel reported in Reference 15. There are no dynamic strength data available for the HS fragment material (AISI C-1141). The dynamic strength value of 18 kbars for the HS material is comparable to a value of 16 kbars reported for SAE 4340 steel of similar hardness but slightly larger static yield strength;[15] however, the value for the HS material is larger by a factor of two than reported values for SAE 1040 steel. Application of the factor of 1.45 for the ratio of dynamic to static yield strengths, which is an average of the value of 1.8 reported for SAE 1040 steel[16] and the value 1.1 reported for SAE 4340 steel,[15] to the uniaxial strain static yield value for the HS material (0.0117 mbar) gives 17 kbars for the dynamic yield strength, which is in good agreement with the value of 18 kbars determined in this study.

41. Additional credence to the impact pressures computed by the characteristics code is given by experimental data such as presented in Reference 20, which show that observed initial pressures following impacts of rods and discs are in good agreement with those predicted by one-dimensional theory. However, the pressure is observed experimentally to drop off immediately with distance into the target instead of exhibiting a constant pressure region for some distance into the target as is predicted by one-dimensional hydrodynamic theory.[21]

42. With the particle velocities calculated for the fragment and target at impact (see Figure 32), it was possible to calculate the initial energy partitioning at the time when the shock wave reaches the rear of the fragment as a function of impact velocity based on the one-dimensional considerations of Gault and Heitowit.[22] The results of these calculations are given in the following tabulation, in which the values are normalized to the initial projectile kinetic energies and expressed as a percentage:

| Impact Velocity V cm/μsec | Energy Value, percent | | | |
|---|---|---|---|---|
| | $KE_P$ | $\Delta E_P$ | $KE_T$ | $\Delta E_T$ |
| 0.03048 | 84.3 | 0.7 | 7.5 | 7.5 |
| 0.09144 | 79.3 | 1.2 | 9.75 | 9.75 |
| 0.1524 | 75.6 | 1.7 | 11.35 | 11.35 |
| 0.21366 | 72.2 | 2.3 | 12.25 | 12.25 |

In the tabulation, $KE_P$ is the residual fragment kinetic energy, $\Delta E_P$ is the increase in fragment internal energy, $KE_T$ is the kinetic energy imparted to the target material, and $\Delta E_T$ is the increase in internal energy of the target material. While the above results are valid only for the initial energy partition at impact, they qualitatively confirm many of the phenomenological observations of the experimental program. For example, the increasing percentage of energy transferred to the target as kinetic energy with increasing impact velocity is consistent with the increasing quantity of target ejecta and cratering observed. The increasing percentage of energy transferred to the target as internal energy with increasing impact velocity is consistent with and accounts for the increased sand comminution observed as the impact velocity increases. Also, the observed elevated temperatures in the target at the higher impact velocities are consistent with the increasing percentages of energy transferred to internal energy of the fragment and target. The increasing percentage of energy transferred to internal energy of the fragment raises the temperature and serves as a driving mechanism for the material flow discussed earlier. Further discussion of the details of the energy partition is beyond the scope of this report. References 9, 22, and 23 discuss the initial and late-time energy partitioning and present the process involved in greater detail for fragment impact.

## Correlation of Experimental Results with Penetration Model Predictions

43. Rohani[2] correlated his experimental results with the predictions of an analytical penetration model. The model is based on the

dynamic cavity expansion penetration theory of Ross and Hanagud and has been extended by WES to treat arbitrary fragment nose shapes, to treat layered targets, and to use a complete pressure-density relation for the target.[24,25] He concluded that the WES penetration model could be used to predict or reasonably bound the penetration depths of high-velocity fragments into soil targets. On this basis, the penetration model was used in an attempt to duplicate the experimental results of Figures 15 and 22 and to investigate the feasibility of bounding the penetration depths.

44. For the penetration model calculations, the initial target densities of Tables 1 and 2, the pressure versus relative density relation of Figure 31 for sand, and the values of Young's modulus, strain-hardening modulus, and yield strength recommended by Rohani (Table 7, Reference 2) for the dense sand targets were used to characterize the targets. The fragments were characterized by their mass, presented frontal area, and a function describing their nose shape. For an upper-bound calculation, it seemed appropriate to use the initial mass $M_i$ and the initial frontal area $A_i$ ; for the lower-bound calculation, it was assumed that all deformation and mass loss would occur at the instant of impact, and the final mass $M_f$ and final frontal area $A_f$ were used for the calculation. Assuming a hemispherical nose shape results in a higher upper-bound estimate than that obtained by assuming a blunt nose shape. For the lower-bound estimates, the assumption of a hemispherical nose is consistent with the observed deformed shape of the recovered fragments. Correlations of the experimental values with the calculated penetration model upper- and lower-bound estimates for each test are presented in Figures 33 and 34.

45. In all cases, the experimental penetration depths from these tests (Tables 1 and 2) are bounded by the penetration model upper- and lower-bound estimates. In fact, in most of the cases the

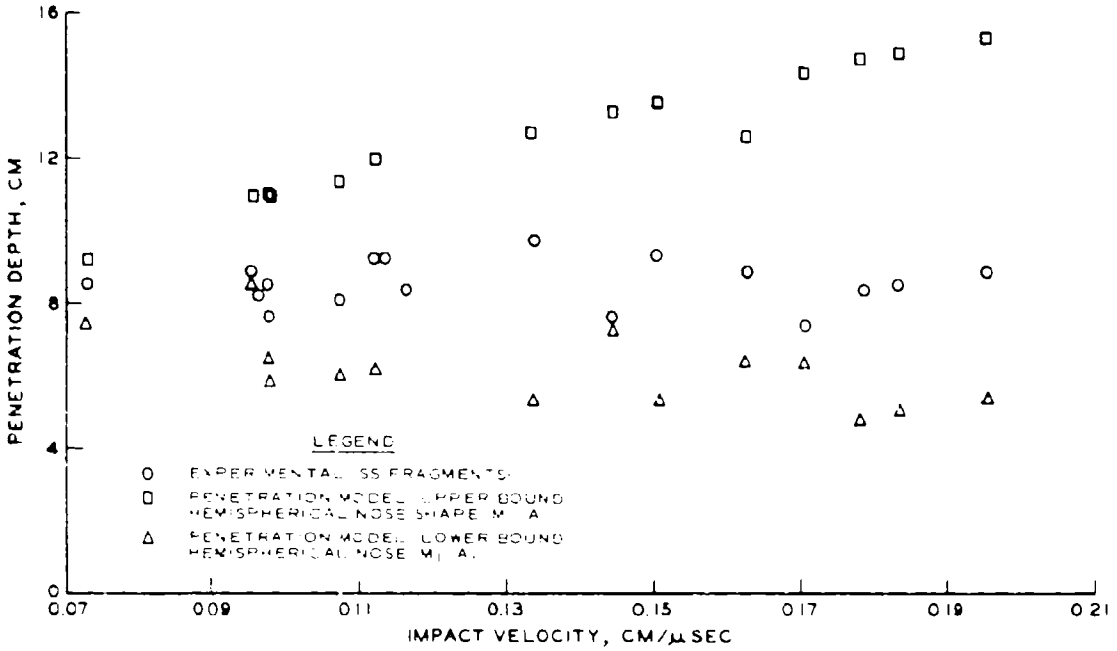


Figure 33. Correlations of experimental penetration results for SS fragments with upper- and lower-bound penetration model calculations

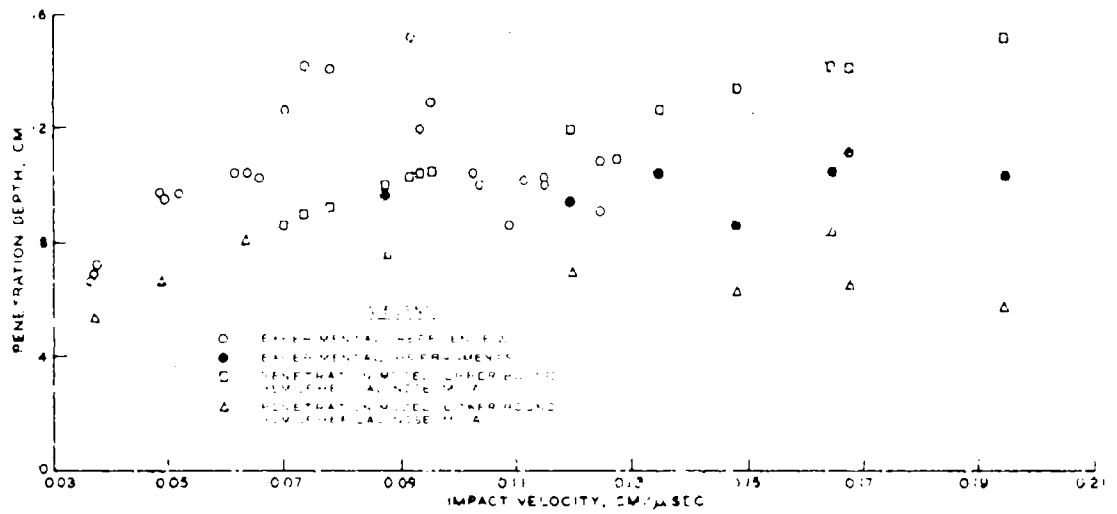


Figure 34. Correlations of experimental penetration results for HS fragments with upper- and lower-bound penetration model calculations

experimental value is approximated by the mean of the upper- and lower-bound estimates. This trend is indicative of the fact that the physical mechanisms actually occurring (perhaps as proposed in Figure 23) are intermediate to the extreme assumptions used to make the upper- and lower-bound estimates. The data from Reference 2 in Figure 34 are not bounded by the upper-bound penetration model calculations. It was demonstrated in a parameter study in Reference 2, however, that the dense sand penetration values could be bounded by a different (and perhaps better) selection of target material properties for use in the model calculations.

## PART V: CONCLUSIONS AND RECOMMENDATIONS

### Conclusions

46. This report documents the design and capabilities of the WES high-velocity powder gun. The powder gun has been calibrated (with nominal 3-g fragments) over the velocity range 0.05 to 0.222 cm/μsec (1650 to 7280 fps). With improvement of the bore evacuation system, it is considered feasible to attain 0.244 cm/μsec as an upper limit. A lower limit of 0.03 cm/μsec is considered possible with faster burning powders. The gun is versatile and easy to use and has many potential applications for study of the effectiveness of various components of fortification systems (such as soil, wood, fabric, concrete, steel, plastic, etc.) in defeating small-arms munitions and fragment-simulating projectiles. The firing rate (number of tests per day) is limited only by required target preparation time.

47. The results of 27 penetration tests of cylindrical fragments into dense sand targets are presented. The following conclusions and observations are based on these results:

a. Dense sand is an effective medium for stopping high-velocity projectiles or fragments.

b. The penetration depth attained by high-velocity projectiles or fragments in dense sand is not a monotonically increasing function of impact velocity but tends to remain constant after a critical impact velocity* (which depends on the strength and hardness of the fragment material) is exceeded. The critical impact velocity increases as the strength of the fragment material increases. The overall shape of the penetration depth versus impact velocity curve depends in a very complex manner on the details of fragment deformation and mass loss during penetration, which in turn depend on the fragment material properties.

c. With reference to Figure 1, the data of this report and Reference 2 demonstrate that the behavior indicated by curve CDE does not occur for the steel and brass fragments tested. Although the desired maximum impact velocity of 0.274 cm/μsec (9000 fps) was not achieved in this study, the observations of penetration depth and fragment mass loss and deformation (at impact velocities up to

---

* Velocity at which deformation of the fragment is initiated.

0.2 cm/μsec) suggest that the constant penetration depth represented by curve CDF in Figure 1 is an upper bound for the penetration depths which would be observed at higher impact velocities (> 0.2 cm/μsec).

d. The fragment penetration process results in comminution or crushing of the sand grains. This is reflected in an upward shift of the gradation curves, with increasing impact velocity, relative to the gradation curve of the parent material.

e. The percent finer by mass data for the HS fragments (Figure 29) indicate a jump in value at about the same impact velocity as the critical velocity for the HS material discussed in subparagraph 47b above. This increase indicates a jump in the energy being transferred to the comminution process at this velocity.

f. A one-dimensional analogy of the fragment penetration process is a valuable aid in elucidating the phenomenology of penetration. Also, the one-dimensional analogy gives reliable values for the impact pressures and particle velocities.

g. The WES penetration model can be used to bound the penetration depths of small projectiles and fragments in dense sand.

## Recommendations

48. It is recommended that the vacuum system of the high-velocity powder gun be improved and that the feasibility of using faster burning powders be investigated in order to extend the useful velocity range of the gun for fragment impact and penetration studies. A high-speed camera should be used if possible in future tests to study methods of improving sabot and fragment separation.

49. All future penetration tests into soils, particularly sands, should incorporate posttest grain-size analyses into the test program. Fragment deformation and mass loss measurements should be continued methodically in all future tests also. Radiographs of the targets prior to fragment recovery should be obtained if feasible in future testing programs.

50. It is desirable that a test program be undertaken to verify the shape of the penetration curve in Figure 21 with carefully controlled tests in a single test series over the velocity range 0.03 to 0.21 cm/μsec.

## REFERENCES


1. Reeves, G. N. and Rohani, B., "Fragment and Projectile Penetration Resistance of Soils; Literature Review and Preliminary Theoretical Study of Soils as a Fortification Material," Miscellaneous Paper S-71-12, Report 1, Jul 1971, U. S. Army Engineer Waterways Experiment Station, CE, Vicksburg, Miss.

2. Rohani, B., "Fragment and Projectile Penetration Resistance of Soils; High-Velocity Fragment Penetration into Laboratory-Prepared Soil Targets," Miscellaneous Paper S-71-12, Report 2, Jun 1973, U. S. Army Engineer Waterways Experiment Station, CE, Vicksburg, Miss.

3. Brown, J. W. and Dykes, W. G., "Army Aircraft Protective Structures Designs; Response of Selected Materials to High-Speed Fragment Impact," Technical Report N-69-8, Report 3, Aug 1971, U. S. Army Engineer Waterways Experiment Station, CE, Vicksburg, Miss.

4. Tate, A., "Further Results in the Theory of Long Rod Penetration," Journal of the Mechanics and Physics of Solids, Vol 17, 1969.

5. Stacey, F. D., Physics of the Earth, John Wiley and Sons, Inc., 1969.

6. Clough, G. W., An Investigation of the Shear Strength of Sand at High Pressures, MS Thesis submitted to Georgia Institute of Technology, October 1964.

7. Vesic, A. S., Clough, G. W., "Behavior of Granular Materials under High Stresses," Journal of the Soil Mechanics and Foundations Division, ASCE, May 1968.

8. Allen, W. A., Mayfield, E. B., Morrison, H. L., "Dynamics of a Projectile Penetrating Sand," Journal of Applied Physics, Vol 28, No. 3, March 1957.

9. Braslau, D., "Partitioning of Energy in Hypervelocity Impact Against Loose Sand Targets," Journal of Geophysical Research, Vol 75, No. 20, 10 Jul 1970.

10. Hakala, W. W., Resistance of a Granular Medium to Normal Impact of a Rigid Projectile, PhD Dissertation submitted to Virginia Polytechnic Institute, Jun 1965.

11. Thompson, L. J., "Dynamic Penetration of Selected Projectiles into Particulate Media," Development Report SC-DR-66-376, 1966, Sandia Corporation, Albuquerque, N. M.

12. Dynamic Response of Materials to Intense Impulsive Loading, edited by P. C. Chou and A. K. Hopkins, Air Force Materials Laboratory, Wright Patterson AFB, Ohio, Aug 1972.

13. Taylor, G. I., "The Use of Flat-Ended Projectiles for Determining Dynamic Yield Stress," Proceedings of the Royal Society, Vol 194A, Sep 1948.

14. Wilkins, M. L., Guinan, M. W., "Impact of Cylinders on a Rigid Boundary," Journal of Applied Physics, Vol 44, No. 3, Mar 1973.

15. Jones, O. E., Nielson, F. W., Benedict, W. B., "Dynamic Yield Behavior of Explosively Loaded Metals Determined by a Quartz Transducer Technique," Journal of Applied Physics, Vol 33, No. 11, Nov 1962.

16. Duvall, G. E., Response of Metals to High Velocity Deformation, edited by P. W. Shweman and V. F. Zackay, Interscience, New York, 1961.

17. Tate, A., "A Theory for the Deceleration of Long Rods After Impact," Journal of the Mechanics and Physics of Solids, Vol 15, pp 387 to 399, 1967.

18. Butler, D. K., "Analysis of Projectile Penetration into Aroclor," U. S. Naval Ordnance Laboratory, NOLTN8916, Jul 1970.

19. Van Thiel, M., Editor, Compendium of Shock Wave Data, Lawrence Radiation Laboratory, UCRL-50108 Vol 1, Supplement 1, October 1967.

20. Eichelberger, R. J., "Hypervelocity Impact," Behavior of Materials Under Dynamic Loading, edited by N. J. Huffington, Jr., American Society of Mechanical Engineers, 1965.

21. Erkman, J. O., Christensen, A. B., Fowles, G. R., "Attenuation of Shock Waves in Solids," Technical Report No. AFWL-TR-66-12, May 1966, Air Force Weapons Laboratory, Kirtland Air Force Base, N. M.

22. Gault, D. E., and Heitowit, E. D., "The Partition of Energy for Hypervelocity Impact Craters Formed in Rock," Proceedings of the Sixth Hypervelocity Impact Symposium, Cleveland, Ohio, Vol II, Part 2, 1963.

23. Hill, D. R. and Johnson, W. E., "Energy Partitioning During Hypervelocity Impact on Rocks," Dynamic Rock Mechanics, Proceedings of the Twelfth Symposium on Rock Mechanics, edited by J. B. Clark, University of Missouri at Rolla, 1971.

24. Bernard, R. S. and Managhi, G. V., "Development of a Projectile Penetration Theory; Penetration Theory for Shallow to Moderate Depths," Technical Report S-75-[illegible], Report 1, Jun 1975, U. S. Army Engineer Waterways Experiment Station, CE, Vicksburg, Miss.

25. Bernard, R. S., "Development of a Projectile Penetration Theory; Deep Penetration Theory for Homogeneous and Layered Targets," Technical Report S-75-9, Report 2 (in preparation), U. S. Army Engineer Waterways Experiment Station, CE, Vicksburg, Miss.

Table 1

Penetration Test Results with LV System

| Test No. | Target Density $g/cm^3$ | Impact Velocity V, cm/μsec | Penetration Depth P, cm | Frontal Area Enlargement Coefficient $C_A$ | Reduced Mass Coefficient $C_M$ |
|---|---|---|---|---|---|
| SS-DS-LV1 | 1.70 | 0.0976 | 8.48 | 1.95 | 0.97 |
| SS-DS-LV2 | 1.71 | 0.0980 | 7.68 | 2.15 | 0.99 |
| SS-DS-LV3 | 1.69 | 0.1167 | 8.40 | 2.35 | 0.99 |
| SS-DS-LV4 | 1.65 | 0.1134 | 9.22 | 2.31 | 1.00 |
| SS-DS-LV5 | 1.72 | 0.0729 | 8.57 | 1.20 | 0.96 |
| SS-DS-LV6 | -- | -- | -- | -- | -- |
| SS-DS-LV7 | 1.67 | 0.0954 | 8.88 | 1.29 | 0.97 |
| SS-DS-LV8 | 1.74 | 0.0962 | 8.38 | (hit on side) | 0.87 |

Table 2

Penetration Test Results with HV System

| Test No. | Target Density $g/cm^3$ | Impact Velocity V, cm/μsec | Penetration Depth P, cm | Frontal Area Enlargement Coefficient $C_A$ | Reduced Mass Coefficient $C_M$ |
|---|---|---|---|---|---|
| SS-DS-HV1 | 1.69 | 0.1121 | 9.24 | 2.26 | 1.00 |
| SS-DS-HV2 | 1.76 | 0.1449 | 7.68 | 1.44 | 0.73 |
| SS-DS-HV3 | 1.78 | 0.1339 | 9.78 | 2.69 | 0.91 |
| SS-DS-HV4 | 1.78 | 0.1624 | 8.85 | 1.50 | 0.60 |
| SS-DS-HV5 | 1.75 | 0.1072 | 8.14 | 2.22 | 1.00 |
| SS-DS-HV6 | 1.76 | 0.1505 | 9.40 | 3.29 | 0.91 |
| SS-DS-HV7 | 1.75 | 0.1707 | 7.45 | 2.84 | 0.98 |
| SS-DS-HV8 | 1.75 | 0.1786 | 8.33 | 2.78 | 0.61 |
| SS-DS-HV9 | 1.75 | 0.1836 | 8.53 | 2.00 | 0.50 |
| SS-DS-HV10 | 1.75 | 0.1958 | 8.81 | 3.57 | 0.84 |
| HS-DS-HV11 | 1.72 | 0.1481 | 8.67 | 2.37 | 0.91 |
| HS-DS-HV12 | 1.76 | 0.1194 | 9.58 | 1.82 | 0.96 |
| HS-DS-HV13 | 1.75 | 0.0876 | 9.63 | 1.34 | 0.98 |
| HS-DS-HV14* | 1.75 | 0.1348 | 10.50 | -- | -- |
| HS-DS-HV15 | 1.72 | 0.1648 | 10.57 | 1.36 | 0.75 |
| HS-DS-HV16 | 1.74 | 0.1946 | 10.44 | 1.80 | 0.55 |
| SS-DS-HV17 | 1.74 | 0.1628 | 10.01 | 2.23 | 0.69 |
| HS-DS-HV18 | 1.75 | 0.1679 | 11.30 | 1.43 | 0.58 |
| B-DS-HV19 | 1.75 | 0.1169 | 10.67 | 1.52 | 0.63 |
| B-DS-HV20 | 1.76 | 0.1802 | 9.37 | -- | 0.16 |

* Sabot failed to separate.

**In accordance with ER 70-2-3, paragraph 6c(1)(b), dated 15 February 1973, a facsimile catalog card in Library of Congress format is reproduced below.**

Butler, Dwain K

Development of a high-velocity powder gun and analysis of fragment penetration tests into sand, by Dwain K. Butler. Vicksburg, U. S. Army Engineer Waterways Experiment Station, 1975.

57 p. illus. 27 cm. (U. S. Waterways Experiment Station. Miscellaneous paper S-75-27)

Prepared for Office, Chief of Engineers, U. S. Army, Washington, D. C., under Project 4A161102B52E, Task 04, Work Unit 013.

References: p. 56-57.

1. Fragmentation. 2. Penetration tests (Soils). 3. Powder guns. 4. Projectiles. 5. Sands. I. U. S. Army. Corps of Engineers. (Series: U. S. Waterways Experiment Station, Vicksburg, Miss. Miscellaneous paper S-75-27)

TA7.W34m no.S-75-27